Shear-banding in surfactant wormlike micelles: Elastic instabilities and wall slip

M.A. Fardin,[1,2] T. Divoux,[3] M.A. Guedeau-Boudeville,[1] I. Buchet-Maulien,[4] J. Browaeys,[1] G.H. McKinley,[2] S. Manneville,[3,5] and S. Lerouge[1,*]

[1] *Laboratoire Matière et Systèmes Complexes, CNRS UMR 7057 Université Paris Diderot, 10 rue Alice Domont et Léonie Duquet, 75205 Paris Cédex 13, France*

[2] *Department of Mechanical Engineering Massachusetts Institute of Technology, 77 Massachusetts Avenue, MA 02139-4307 Cambridge, USA*

[3] *Université de Lyon, Laboratoire de Physique, CNRS UMR 5672 École Normale Supérieure de Lyon, 46 Allée d'Italie, 69364 Lyon cedex 07, France*

[4] *Laboratoire Itodys, CNRS UMR 7086 Université Paris Diderot, 15 rue Jean de Baïf, 75205 Paris Cédex 13, France*

[5] *Institut Universitaire de France*

(Dated: November 26, 2011)

We report on the flow dynamics of a wormlike micellar system (CPCl/NaSal/brine) undergoing a shear-banding transition using a combination of global rheology, 1D ultrasonic velocimetry and 2D optical visualisation. The different measurements being performed in a single Taylor-Couette geometry, we find a strong correlation between the induced turbid band observed optically and the high shear rate band. This correspondence reveals that fluctuations observed in the 1D velocity profiles are related to elastic instabilities triggered in the high shear rate band: 3D coherent (laminar) flow and 3D turbulent flow successively develop as the applied shear rate is increased. The specific characteristics of the resulting complex dynamics are found to depend on subtle changes in the sample, due to temporary light exposure. The CPCl molecules exhibit a photochemistry mainly influenced by the photo-induced cleavage of the pyridine ring that yields an unstable aldehyde enamine, which further decays by thermally activated processes. The products of the reaction possibly build up a lubrication layer responsible for pathological flow dynamics. Overall, our results bridge the gap between previous independent optical and local velocity measurements and explain most of the observed fluctuations in terms of a sequence of elastic instabilities which turns out to be widespread among semidilute wormlike micellar systems.

INTRODUCTION

Shear-banding is ubiquitous in complex fluids and related to the organization of the flow into macroscopic bands bearing different viscosities and local shear rates and stacked along the velocity gradient direction. This flow-induced transition towards a heterogeneous flow state has been reported in a variety of systems [1], including wormlike micellar solutions [2, 3], telechelic polymers [4, 5], emulsions [6, 7], clay suspensions [6, 8, 9], colloidal gels [10], star polymers [11] granular materials [12], or foams [13]. In wormlike micelles, these shear localization effects are associated with a stress plateau that separates two increasing branches in the flow curve (i.e. the shear stress σ vs shear rate $\dot{\gamma}$ curve). In the plateau region, the flow splits into two shear bands, the relative proportions of which depend on the applied shear rate, usually assumed to follow a simple lever rule $\dot{\gamma} = (1-\alpha_h)\dot{\gamma}_1 + \alpha_h\dot{\gamma}_2$, where α_h is the proportion of the high shear rate band and $\dot{\gamma}_1$ and $\dot{\gamma}_2$ are the lower and upper limits of the stress plateau. The parts of the flow curve for $\dot{\gamma} < \dot{\gamma}_1$ and $\dot{\gamma} > \dot{\gamma}_2$ are usually called the low and high shear rate branches respectively. Beyond this classical 1D shear-banding scenario,which is typically observed through time-averaged velocity measurements [14], fluctuations in the global rheological data (shear and normal stresses) or in the local quantities (local flow field and supramolecular ordering) have been reported in many different micellar solutions ([3, 15] and Refs. therein) using time and space-resolved techniques [16, 17]. 1D time-dependent velocimetry experiments have revealed that this fluctuating behavior may arise from interplay between wall slip and shear-banding [18–20], hence highlighting the crucial role of the boundary conditions, which has also been noticed in simulations [21]. More complex pictures also have emerged from 2D flow visualisations, with evidence of an interfacial instability associated with the development of Taylor-like vortices in the induced band and stacked along the vorticity direction [22–24]. A complementary study [25], conducted on the homogeneous flow recovered on the high shear rate branch also revealed a flow instability reminiscent of the purely elastic turbulence usually observed in polymer solutions [26, 27]. Very recently, purely elastic turbulence was also characterised in yet another surfactant system [28]. This trend of research suggests that the fluctuations observed so far from 1D signals may result from purely elastic instabilities [29]. Observations indicate that the instability is focused in the induced band, leading to 3D secondary flows, coherent or turbulent, during and beyond the shear-banding regime, *i.e.* when

* Corresponding author ; sandra.lerouge@univ-paris-diderot.fr

$\alpha_h < 1$ and when $\alpha_h = 1$. Theoretically, attempts to rationalize the 3D character of the shear-banding flow have been made through linear stability analysis with respect to axisymmetric [30, 31] and non-axisymmetric [32] disturbances in the framework of the diffusive Johnson-Segalman (dJS) model [33–36]. The elastic instability hypothesis has been confirmed, with a possible interplay between bulk and interface modes, depending in particular on the curvature of the streamlines of the base flow [31, 32].

The most recent results indeed suggest that shear-banding flows can be perturbed by elastic instabilities. But most of the experiments that helped to build this picture were performed on a single system consisting of a semi-dilute aqueous mixture of cetyltrimethylammonium bromide and sodium nitrate (CTAB/$NaNO_3$). In the present paper, we focus on a wormlike micellar solution made of 10% cetylpyridinium chloride (CPCl) and sodium salicylate (NaSal) in NaCl brine. This system, originally studied by Berret et al. [37, 38] has been intensively investigated these last years, especially by the Wellington group and is now well-known to exhibit fluctuations [17]. Using nuclear magnetic resonance (NMR) velocimetry, large fluctuations of the 1D velocity profiles were observed as the system was quenched in the plateau region, the size of the high shear rate band being driven by the degree of slip at the moving wall [18, 39, 40]. Depending on the batch, the fluctuations could adopt either a quasi-random or a periodic character and were correlated with the fluctuations in the shear stress time series. Moreover, the proportion of the high shear rate band increased linearly with the applied shear rate, following the simple lever rule. However, in a recent study [20] performed by the same group, the authors observed a different picture, with strong departure from the standard lever rule. In Taylor-Couette flow geometries with smooth or rough boundary conditions, they found that the local shear rates in each band increased with the applied shear rate (with nonetheless a rapid saturation in the low shear band), while the relative proportions of the bands remained essentially constant. This anomalous behavior has been ascribed to fluctuating slip dynamics together with subtle changes in the sample inherent to the batch [41]. Also, this anomalous behavior was ascribed to the use of moderate shear rate increments rather than quenches, which were preferred in earlier studies. The local shear rate in the high shear rate band was also found to exhibit time-dependent variations, suggesting instability of this band. Besides, a 2D extension of the NMR velocimetry technique provided evidence of fluctuations of the azimuthal velocity along the vorticity direction with a characteristic length scale on the order of a centimeter, *i.e.* an order of magnitude larger than the gap [20]. The 10% CPCl/NaSal system has also been used recently to explore the effects of the boundary conditions (BC) on the shear-banding flow by means of time-resolved ultrasonic velocimetry (USV) [19]. Slip was observed whatever the boundary conditions (smooth or rough). However, with rough (or 'stick') BC, shear-banding with large fluctuations in the high shear rate band developed whereas, with smooth (or 'slip') BC, wall slip competed with shear-banding leading to a two-bands structure that was only intermittently observed.

To summarize, all the recent studies on the 10% CPCl/NaSal system evidenced fluctuations. In almost all cases, the fluctuations were rationalized by the authors of the studies by invoking a correlation between the shear-banding structure and the dynamics of wall slip. But the possibility that secondary flows triggered by elastic instability were at the origin of fluctuations was never considered thoroughly.

In the present paper, we investigate the Taylor-Couette flow properties of 10% CPCl/NaSal/brine samples using global rheology, 1D ultrasonic velocimetry and 2D optical visualisations. Our main goal is to understand more clearly the origin of the fluctuations reported in this system, and the discrepancies between different batches. We wish to be able to distinguish the impact of wall slip from the impact of secondary flows triggered by elastic instabilities. One of the unique features is the use of a single flow geometry that enables a precise correlation for all types of experiments. We observe that two samples prepared from the same batch and showing quasi-similar global rheological properties, can exhibit discrepancies in their shear-banding flow dynamics. For the first time, we build a solid rationale to explain a possible origin for the discrepancies. Our working hypothesis relies on the sensitivity of the CPCl/NaSal solutions to ambient light exposure that may induce subtle changes at the molecular scale. To allow for a systematic study, we artificially trigger modifications in the samples using UV irradiation protocols. 1D USV measurements reveal that the magnitude of wall slip is larger for irradiated samples suggesting that the interaction with the walls is modified by the products of photochemical reactions. We describe in the Electronic Supplementary Information how the cetylpyridinium chloride surfactant molecules exhibit a photochemistry mainly influenced by the photo-induced cleavage of the pyridine ring that yields an unstable aldehyde enamine, which further decays by thermally activated processes. The products of the reaction possibly build up a lubrication layer responsible for pathological flow dynamics.

Overall, the use of a single flow geometry to perform 2D optical visualisation and 1D velocimetry demonstrates an unequivocal correspondence between the turbid band observed using the former technique and the high shear rate band observed using the latter. This correlation, together with the identification of a source of discrepancies between samples, enables us to re-interpret fluctuations observed in 1D velocity profiles. Our results demonstrate that the shear-banding flow of the 10% CPCl/NaSal is unstable due to the elastic instability of the high shear rate band. The band is found to undergo successive instabilities as the applied shear rate is increased, with the development of a 3D coherent secondary flow followed

by a transition toward a turbulent state. The particulars of the scenario are different from the ones seen in the CTAB/$NaNO_3$ system, but it can be very well rationalized in the same elastic instability framework. The presence of wall slip is confirmed, but its role in explaining the fluctuations is shown to be secondary.
The paper is organized as follows. In section I, we highlight the preparation of the samples, the irradiation protocols and the different experimental techniques employed. Section II is dedicated to a description of preliminary observations, which confirm the possibility of discrepancies between fresh and older samples and show that sample alteration can be artificially accelerated by UV light irradiation. Section III describes in detail the behaviors of fresh and irradiated samples, showing the correspondence between 2D optical visualisation and 1D velocimetry. Comparisons with specific points of the literature also appear in this section. In section IV, we discuss the consequences of our studies in clarifying the differences between the shear-banding flow of the 10% CPCl/NaSal system with respect to the rationale previously built around the CTAB/$NaNO_3$ system. We discuss the role of elastic instabilities as the principal cause of fluctuations, as well as the lesser but genuine impact of wall slip on shear-banding and its interplay with elastic instabilities. Finally, we conclude in section V.

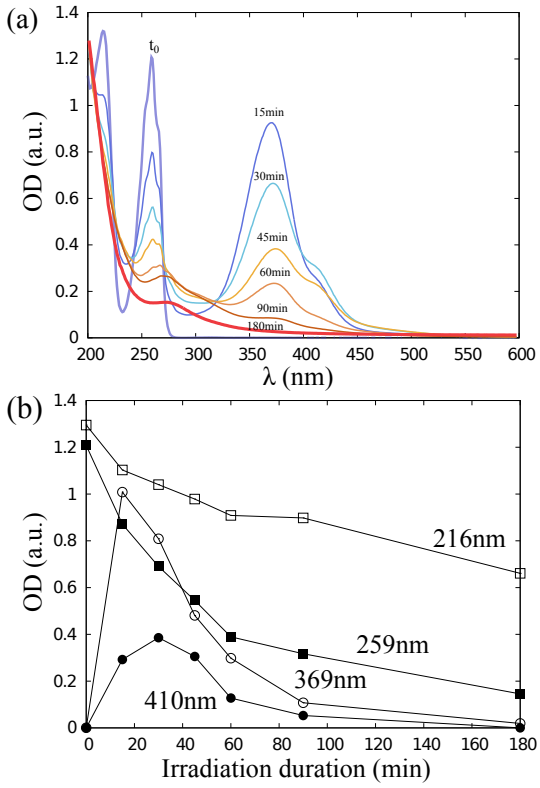

FIG. 1. Photochemical kinetics for various irradiation durations. (a) UV-visible spectra of 0.05$wt.$% CPCl solutions for irradiation times of 0, 15, 30, 45, 60, 90 and 180 min. (b) Optical density (OD) as a function of the irradiation duration for four wavelength 216 nm, 259 nm, 369 nm and 410 nm.

I. MATERIALS AND METHODS

A. Materials

The micellar samples were made of 8.09 $wt.$% (0.238 M) cetylpyridinium chloride (CPCl) with 1.91 % (0.119 M) sodium salycilate (NaSal) in water with 0.5 M sodium chloride (NaCl). In the rheology literature, this solution is usually called CPCl 10 % for the sum of the surfactant (CPCl) and co-surfactant (NaSal) weight fractions [2, 3]. The CPCl and NaCl were purchased from Sigma-Aldrich and the NaSal from Acros-Organics. The CPCl is in a mono-hydrated form. Therefore, we took into account the water molecule to compute the weight fraction.
CPCl is a surfactant whose hydrophilic head is essentially formed by a pyridine ring, C_5H_5N, which is known to be particularly sensitive to light. In aqueous solution, the pyridine ring can be opened by UV radiation, close to the pyridine absorption band at 253.7nm [42, 43]. Photohydration of pyridine cleaves the ring and produces aldehyde enamine (5-amino-2,4-pentadienal). The photo-induced cleavage reaction is usually reversible in aqueous solution, leading to an equilibrium between ring cleavage and ring closure. However in very viscous polymer solutions the cleavage reaction becomes irreversible [44]. The photo-induced cleavage can be measured on the UV-visible spectra given in Fig. 1 and is further discussed in the ESI, where we demonstrate that an essentially irreversible reaction also occurs in CPCl surfactant solutions.

The first step is the cleavage of the ring given by the following reaction:

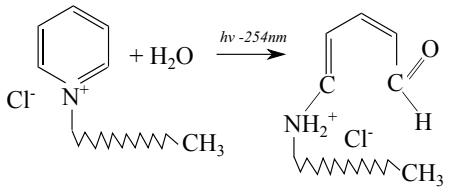

Like in the pure pyridine case, the cleavage yields an unstable aldehyde enamine, which further decays by thermally activated processes. The final products seem to include the free fatty hexadecane tails of the original surfactant.
To quantify the effects of the producs of the photochemical reactions, we distinguished three kind of samples, depending on the light exposure conditions.

- the 'original' sample (OS) kept in a container preventing ambient light exposure.
- the 'old original' sample (O-OS) placed in a transparent container. The designation 'old' refers to the fact that, in course of time, this sample takes a

light yellow colouring (see ESI), due to temporary exposures of the transparent container to ambient light preceding each rheological test.

- the 'irradiated' sample (IS) taken from the OS batch then exposed to an UV light irradiation at 254 nm corresponding to the absorption band of the pyridine ring [42]. The irradiation was performed at 40°C for four hours on a 30 mL micellar solution laid out in a crystalliser, with a UV pen ray lamp placed horizontally at approximately 1-2 cm of the solution stirred by a magnetic bar. We homogenize the exposure and increase the irradiation intensity by covering the set-up with aluminium foil, brilliant face turned towards the interior. In the ESI, we refer to this protocol as 'protocol 2'. The aim of the irradiation protocol is to reproduce artificially, on shorter time scales, the changes observed in the O-OS. The IS is then kept in a container preventing ambient light exposure.

All the samples were stored at 35°C in an oven. In this study, the temperature for experiments is fixed at $T = 21.5$°C. Note also that if the results presented in the paper mostly come from a single set of experiments, the behavior described are reproducible and have been reproduced at several occasions in the past two years, and by different experimenters.

B. Methods

1. Cylindrical Couette geometry

Experiments were performed in two identical transparent small-gap cylindrical Couette devices with smooth walls, also referred to as Taylor-Couette (TC) cells in the following. These cells were adapted either for direct observations of the velocity gradient-vorticity plane (r, z) or for ultrasonic velocimetry of the primary flow in the gap $v_\theta(r)$ at a given location along the vorticity axis. In all experiments, only the inner cylinder was rotating and its axis was adapted to a stress-controlled rheometer (Physica MCR301). A precise description of the TC device used for optical visualisations is given in Sup. Fig. 1. In the cell adapted for ultrasonic velocimetry, the only modification of the design is the enlargement of the water thermostatic bath around the outer fixed cylinder, to allow enough space for the ultrasound transducer. In all experiments, the top of the cell was closed by a small plug which limits the destabilization of the free surface of the fluid at high strain rates [23]. A home-made solvent trap was also used to limit evaporation. The dimensions of the TC device are as follows: inner radius $R_i = 13.33$ mm, height $h = 40$ mm and gap $e = 1.13$ mm .

2. Rheo-optical set-up

In the rheo-optical device, the gap was visualized by using a laser sheet (wavelength 632.8 nm) propagating along the velocity gradient axis and extending along the vorticity axis. A digital camera recorded the scattered intensity at 90°, giving a view of the gap in the (r, z) plane. The field of observation was centred at mid-height and varies from 0.5 to 2 cm according to the chosen magnification. We applied a numerical algorithm to each frame in order to detect the interface [23, 24].
Flow vizualizations in the flow-vorticity plane using seeding anisotropic reflective particles (anisotropic mica platelets from Merck at a volume fraction of 6.10^{-5}), were also performed to observe a possible 3D character of the shear-banding flow. In this configuration, the fluid is illuminated by ambient light and the intensity $I(z)$ reflected in the velocity gradient direction is collected on a digital camera (see ref. [24] for further details).

3. Rheo-velocimetry set-up

The velocity of the sample in the flow direction was measured using high frequency ultrasonic speckle velocimetry at an axial position about 15 mm from the bottom of the TC cell. USV is a technique that allows one to access velocity profiles with a spatial resolution of 40 μm and a temporal resolution of 0.02-2 s depending on the applied shear rate. It relies on the analysis of successive ultrasonic speckle signals that result from the interferences of the backscattered echoes of successive incident pulses of central frequency 36 MHz generated by a high-frequency piezo-polymer transducer (Panametrics PI50-2) connected to a broadband pulser-receiver (Panametrics 5900PR with 200 MHz bandwidth). The speckle signals are sent to a high-speed digitizer (Acqiris DP235 with 500 MHz sampling frequency) and stored on a PC for post processing using a cross-correlation algorithm that yields the local displacement from one pulse to another as a function of the radial position r across the gap. One velocity profile is then obtained by averaging over typically 1000 successive cross-correlations. Full details about the USV technique may be found in [45]. For these velocimetry experiments, 0.3 $wt.\%$ hollow glass spheres were added to the OS and IS, to act as ultrasonic contrast agents [45]. The glass spheres have an average diameter of 6 μm and a density of 1.1 (Potters Industries Inc., UK). The sound speed in our samples was independently measured to be 1555 m/s.

4. Typical protocols

Most of the experimental results presented in this paper are obtained for start-up flows at a known imposed shear rate. Typically, each start-up test was performed

TABLE I. Summary of the linear viscoelastic parameters for 10% CPCl OS, O-OS and IS.

Sample	G_0 (Pa)	τ_R (s)	η_0 (Pa.s)
OS	186±5	0.65±0.05	121±10
O-OS	193±5	0.66±0.05	127±10
IS	210±5	0.52±0.05	109±10

for ten minutes. In between each start-up flow experiment, the sample was allowed to relax and rest without flow for two minutes. When we used the rheo-optical set-up, the samples were free of seeding particles, except if otherwise stated. We performed 2D optical visualisations and simultaneously recorded the global shear stress time series. When we used the rheo-velocimetry set-up, the samples were seeded with the ultrasonic contrast agents. We performed 1D USV and simultaneously recorded the global shear stress time series. Note nonetheless that all the results presented in the paper have also been duplicated using start-up flows at imposed shear stress (*i.e.* creep tests). Except for the particulars of the early time transient response, the same behaviors were observed.

II. PRELIMINARY OBSERVATIONS

At the concentration chosen for this study, far from the isotropic-nematic transition at rest, the solutions are semi-dilute and made of highly entangled wormlike micelles forming an elastic network. The evolutions of the loss and storage moduli indicate that the three solutions OS, O-OS and IS, behave as almost perfect Maxwellian elements over the explored range of frequencies. The elastic modulus G_0 and relaxation times τ_R obtained from fits to the Maxwell model are given in Table I. The three samples present very similar linear properties but with slight quantitative differences : the irradiation process seems to induce a larger elastic modulus and a smaller relaxation time. Computation of the zero shear rate viscosity from $\eta_0 = G_0\tau_R$ shows that the IS is slightly less viscous than the OS and O-OS. Such subtle changes in linear properties for O-OS and IS are most likely due to producs of photochemical reactions, which are discussed in the ESI.

Figure 2 displays the comparison between the steady state shear stress σ as a function of the applied shear rate $\dot{\gamma}$ for the OS, O-OS and IS. The low shear rate branches are not strictly superimposed due to the slight difference in η_0 between the samples, but in any case, after a Newtonian regime, the solutions exhibit shear-thinning. The three experimental flow curves follow quantitatively the same trend : they present two increasing branches separated by a stress plateau at $\sigma_p = 120\pm2$ Pa characteristic of the shear-banding transition, and extending between two critical shear rates $\dot{\gamma}_1$ and $\dot{\gamma}_2$. The *apparent* beginning of the stress plateau $\dot{\gamma}_1$ ranges between $\dot{\gamma}_1^{OS} = 1.3 \pm 0.1$ s^{-1} and $\dot{\gamma}_1^{IS} = 1.5 \pm 0.1$ s^{-1}, while the *apparent* end of the stress plateau $\dot{\gamma}_2$ ranges between $\dot{\gamma}_2^{OS} = 12 \pm 1$ s^{-1} and $\dot{\gamma}_2^{IS} = 17 \pm 1$ s^{-1}.

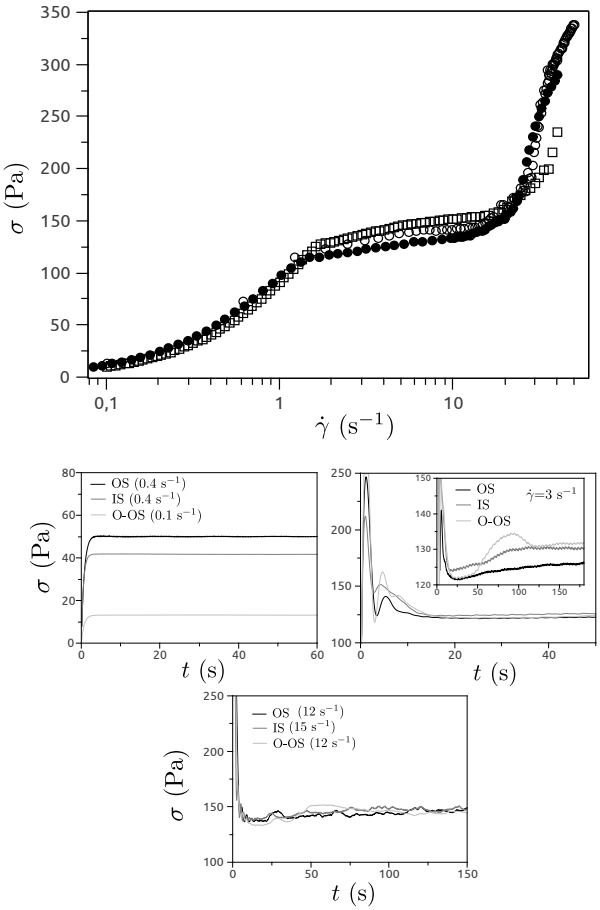

FIG. 2. Top: Semi-logarithmic plot of the steady state apparent flow curves of the OS (closed circles •), O-OS (open circles ○) and IS (open squares □) measured under strain-controlled conditions. The sampling of the shear rate sweep is 120 s per data point. Bottom: transient responses at short times for different applied shear rates along the flow curve.

It is important to stress that the experimental flow curves are *apparent* flow curves, in the sense that the curvature of the geometry, potential secondary flows and wall slip can all have an impact on the measurements, which then do not solely reflect material properties. In particular, the stress plateau is not flat and the shear stress increment between the two extremities ($\Delta\sigma^{OS} \sim 25$ Pa and $\Delta\sigma^{IS} \sim 28$ Pa) is only partially explained by the stress heterogeneity inherent to the cell curvature that leads to a geometrical stress increment $\Delta\sigma$=22 Pa. Beyond concentration effects that can influence the slope, one must also consider the potential influence of secondary flows [23]. Also, above $\dot{\gamma}_2$, the shear stress increases noticeably following an apparent high shear rate branch. We will see in the following that the branch has a purely dynamical origin. This high shear rate branch presents a sharp 'S' shape for the OS. For the IS, this shape seems

broader and the upper part of the 'S' is not reachable due to inclusion of bubbles in the sample. This behavior differs somewhat from the behavior of the O-OS. But let us recall that the effects of light exposure have been artificially enhanced in the IS. As shown in Sup. Fig. 2, if a sample is irradiated only for two hours, its flow curve is in between the O-OS flow curve and the IS, which was irradiated for four hours.

The typical transient responses of the shear stress at short times following a sudden start-up of flow are shown in the subplots of Fig. 2, for various applied shear rates along the flow curve. In the Newtonian region, the expected monoexponential growth is observed. At the beginning of the stress plateau, the response is dominated by a stress overshoot followed by a sigmoïdal decay and/or damped oscillations and a small undershoot preceding the stabilization of the shear stress around a steady state value. As described in details elsewhere [23, 24], the shear stress undershoot contains the mechanical signature of the onset of secondary vortex flows. Such transient stress responses, typical of systems undergoing a shear-banding transition, have been widely observed in the literature [3, 37, 46–49], and we will not comment on it further, as we wish to focus on the local flow behavior of the samples at long times after start-up of flow.

As revealed in Fig. 3 by direct visualisations in the (r, z) plane for various applied shear rates along the stress plateau, the banding structure is not identical in the three samples. As in other wormlike micellar solutions [23, 46, 50–52], the induced band is slightly turbid giving a strong optical contrast between the two bands. In the three cases (OS, O-OS and IS), the system is organized into two macroscopic bands of differing optical properties, separated by an interface that undulates along the vorticity direction. For the OS, we can identify a well-defined wavelength that increases with the applied shear rate, while the pattern appears more complicated for the O-OS and IS. The O-OS and IS behavior are very similar to each other, with an irregular undulation of the interfacial profile and continuous processes of growth and relaxation of turbidity fluctuations further in the gap (see photos at 3, 5 and 8 s^{-1} and movies in the supplementary material). Although the proportion of the induced turbid band and the wavelength of the interface profile seem comparable for the three samples at the beginning of the stress plateau, they become much larger for the OS when the applied shear rate is increased (see photos at 8, 10 and 15 s^{-1}). This observation is consistent with the fact that the interfacial wavelength λ has been found to scale with the proportion of the induced band α_h [53]. In the three samples, as the shear rate is further increased, the induced band undergoes another instability. Typical examples are given at 15 and 17 s^{-1} for the OS, 20 and 25 s^{-1} for the O-OS, and 25 and 35 s^{-1} for the IS. In the same snapshot, we are able to simultaneously observe regions where the bands coexist with an undulated interface and regions where the induced turbid band is destabilized, the flow being locally strongly disordered. Finally, the flow of the OS becomes fully disordered above a shear rate of $\dot{\gamma}$=20 s^{-1}, a picture reminiscent of elastic turbulence [25–28]. Supplementary movies and details given in section III A will help to understand this new flow pattern that we will call *turbulent bursts*. Indeed, an important point here is that the transition towards elastic turbulence starts while the induced band does not fill the entire gap, in contrast to observations in the CTAB/$NaNO_3$ system, where the transition to turbulence occurs on the high shear rate branch [25]. Note that in the three samples, the shear rates that correspond to the onset of turbulent bursts also correspond to $\dot{\gamma}_2$, *i.e.* the up-turn in their flow curve. Therefore, if it was not for the onset of turbulent bursts, the stress plateau would most likely extend to much higher shear rates up to the *true* high shear rate branch, when the proportion of the high shear band would have reached $\alpha_h = 1$.

The conclusion of these preliminary observations is twofold. First, the 10% CPCl micellar solution is seen to exhibit secondary flows. At the beginning of the stress plateau, the secondary flows are reminiscent of the Taylor-like vortex flow previously identified in the CTAB/$NaNO_3$ system [22–25]. But at higher shear rates, and *before* the end of the plateau, we observe the onset of turbulent bursts which temporarily and locally disturb the banding structure (Fig. 3). Second, we have observed some differences in the particulars of this scenario between fresh samples (OS) and aged samples (O-OS). And UV-light irradiation can reproduce the sample alteration, since the behavior of the O-OS and IS are essentially identical. Since the alteration of a sample is difficult to control and can arise over very long times (typically several months), making a systematic study difficult, in the following, we focus only on the comparison between the flow behaviour of the OS and IS.

III. RESULTS

A. 2D optical visualisation–Secondary flow patterns

We now wish to compare in detail the interface dynamics following a sudden step shear rate from rest for the two samples (OS and IS). From the interface profiles detected on each frame, we can build a spatio-temporal diagram that displays in grey levels the interfacial evolution as a function of time and space coordinates. Fig. 4 gathers some of the patterns that we have identified. The z coordinate corresponds to the direction of the cylinder axis. The diagram captures both the transient regime and the asymptotic behaviour. Typically, the inner crests of the interface profile (closer to the inner cylinder) are coded in dark grey while the outer crests

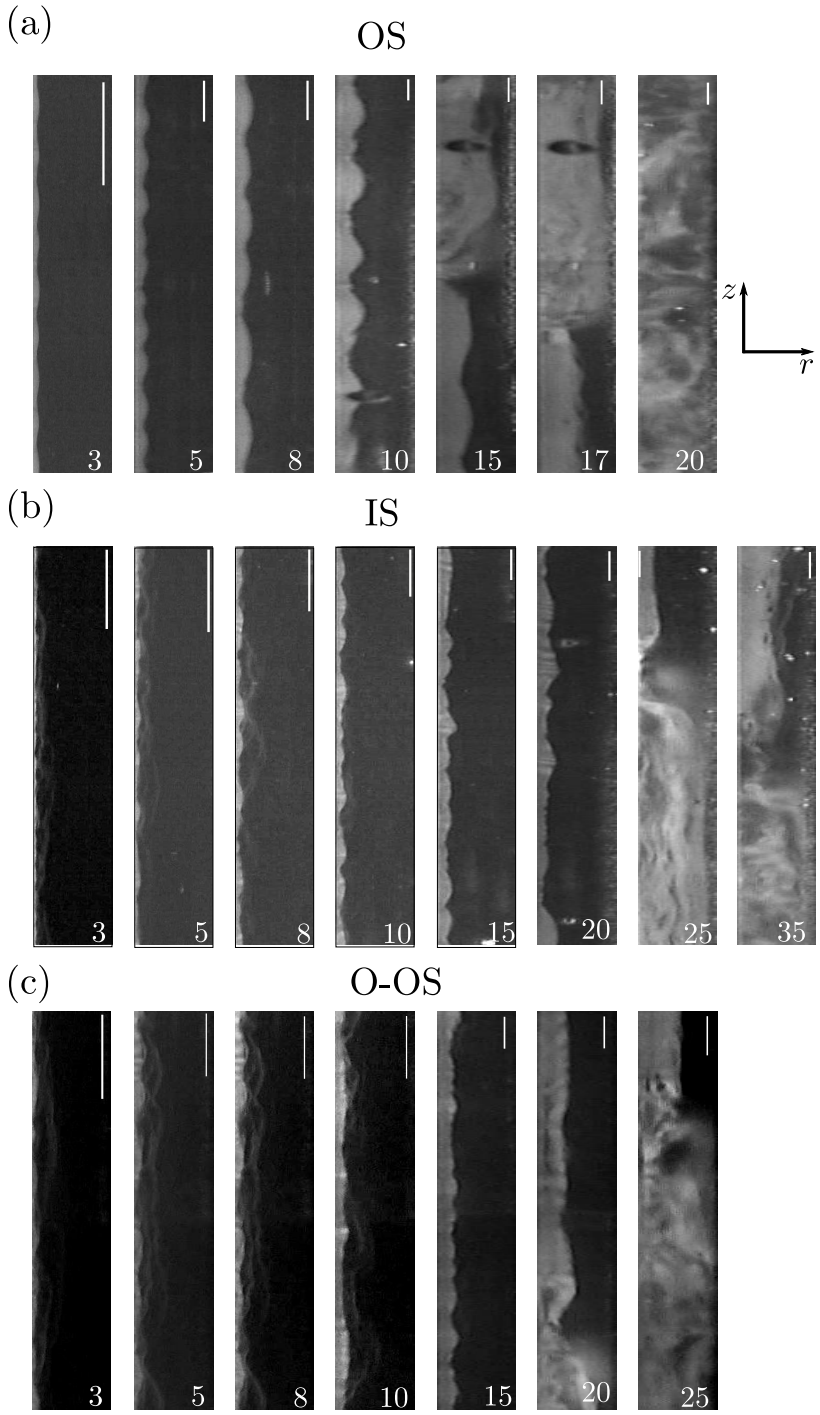

FIG. 3. View of the gap of the TC cell in the (r, z) plane illuminated by a radial laser sheet for different applied shear rates, (a) for the OS, (b) IS and (c) O-OS. The snapshots are extracted from the last 100 s of each step shear rate. The left and right sides of each picture correspond respectively to the inner (rotating) and outer cylinders. The horizontal spatial scale is given by the gap size while the vertical-one is given by the 1 mm white line.

are coded in light gray. Note that in all cases, the interfacial instability is associated with the existence of a secondary vortex flow as illustrated by flow visualisations. The evolution in space and time of the amplitude of the interface along z has been shown previously to be correlated to secondary flows [24]. When the interface exhibits undulations, each wavelength of the interface corresponds to a pair of counter-rotating Taylor-like vortices, mainly localized in the high shear rate band, with inward flows co-localized with the interface inner

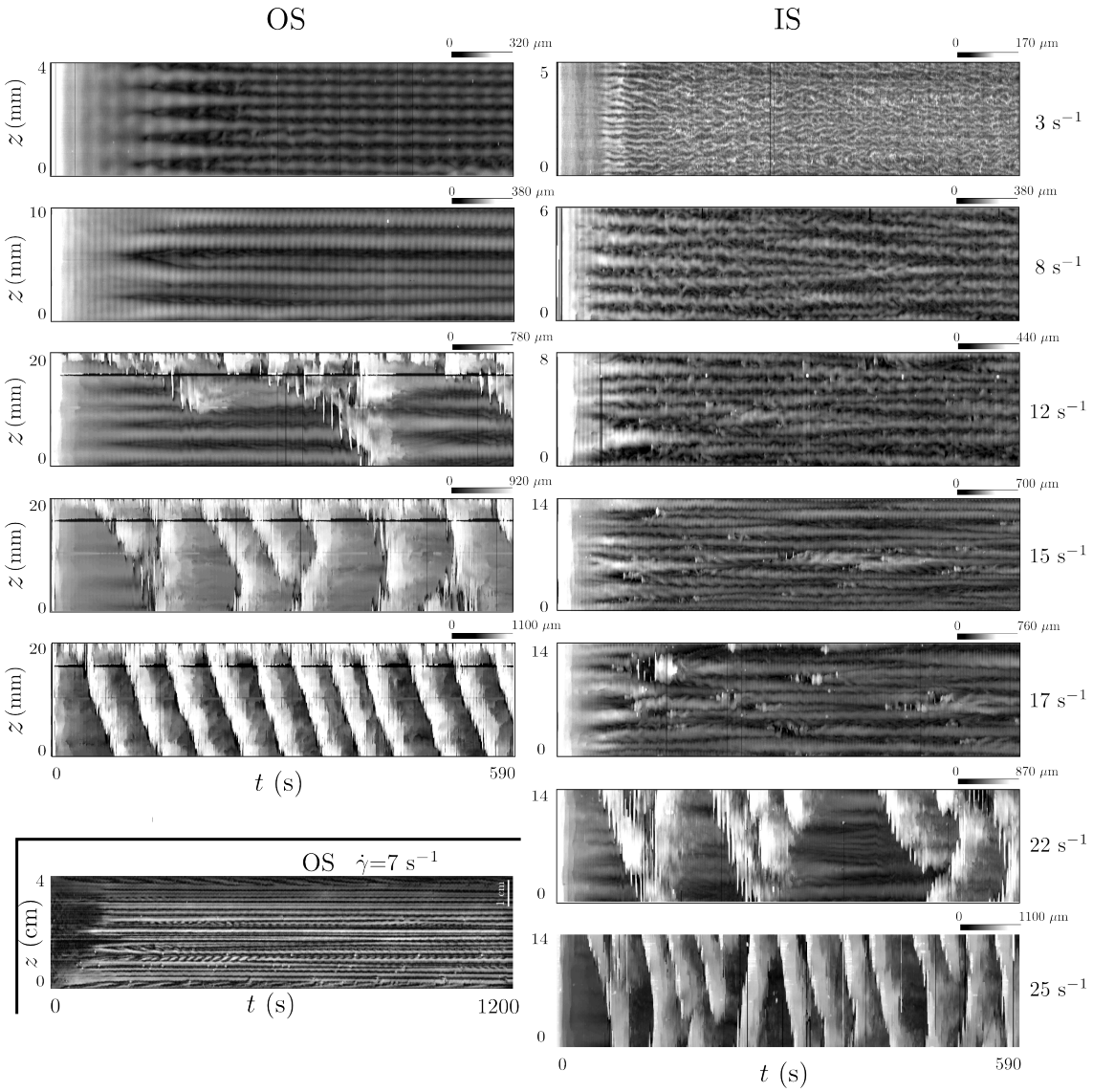

FIG. 4. Spatiotemporal evolution of the position of the interface between bands in response to quenches at different shear rates along the flow curve. The position of the interface in the gap is given in grey levels, with the origin taken at the inner moving wall. The z axis represents the spatial coordinate along the cylinder axis and the size of the field of observation is given at the left-hand side of each diagram. The horizontal axis is the time from the onset of start-up flow. Each spatiotemporal diagram corresponds to 590s. Note that for the OS at 12, 15 and 17 s^{-1}, the horizontal black line on the top of the spatiotemporal diagrams are artefacts due to a bubble stuck in the thermostat around the TC cell. (Bottom left) Intensity distribution $I(z,t)$ reflected in the radial direction by anisotropic mika flakes seeded in the OS for a step shear rate from rest to $\dot{\gamma}$=7 s^{-1}.

crests and outward flows co-localized with the interface outer crests. The spatiotemporal diagram in the bottom left corner of Fig. 4 gives an illustration of the pattern one can obtain by seeding reflective particles in the sample and observing from the outer cylinder. This technique, used in particular by Andereck *et al.* [54] for the study of the inertial Taylor-Couette instability and later by Larson, Shaqfeh, Muller *et al.* [55, 56] for the study of the elastic instability, is sensitive to variations of the radial velocity component [57]. The succession of dark and bright stripes stacked along the vertical direction indicates respectively radial flow and flow perpendicular to the direction of observation. This qualitative flow visualisations, is a good and quick way to gain information on the three-dimensional nature of the flow.

1. *Taylor-like vortex flow and turbulent bursts*

Let us now turn back to a description of the interfacial dynamics, which is clear way to gain information about secondary flow patterns. First, we describe

the interfacial dynamics of the OS. At 3 s^{-1}, after a transient period including construction and migration of the interface, we observe a first growing mode with a wavelength $\lambda \sim 1$ mm followed by a spatial frequency doubling. This change of wavelength is represented by nucleation and growth of new light gray zones in the interface profile around $t \sim 250$ s. At longer times, the interface adopts a spatially stable profile with a wavelength $\lambda = 0.5 \pm 0.03$ mm. As the shear rate is increased, the time needed for the interfacial instability to develop is shorter and the most amplified mode in the initial stages of the instability growth is also the asymptotically dominant mode. Below 12 s^{-1}, the pattern are very similar to those observed in the CTAB/$NaNO_3$ system [23, 24]. From $\dot{\gamma}_2^{OS} = 12$ s^{-1}, the interfacial dynamics are deeply affected by the nucleation of turbulent bursts, which appear as white diagonal patches in the spatiotemporal diagrams. Note that for these shear rates, the field of observation is centered on the upper-half of the TC cell (z=20 mm corresponds to the upper edge of the inner cylinder). This configuration shows that the turbulent bursts seem to nucleate from the upper edge of the TC cell and propagate towards the bottom of the cell. Nevertheless, turbulent events propagating from the bottom of the TC cell are also detectable (see $\dot{\gamma}$=15 s^{-1}). At 12 s^{-1}, the propagation can be rapidly damped in space while, as the applied shear rate is incremented, the turbulent front extends over larger distances along the z direction. Note that the front speed increases with $\dot{\gamma}$. The turbulent bursts have a finite lifetime and their frequency increases with the imposed shear rate (See Sup. Fig. 3). As long as the temporal frequency of the bursts is not too high, the banding structure with the undulated interface has time to reconstruct.

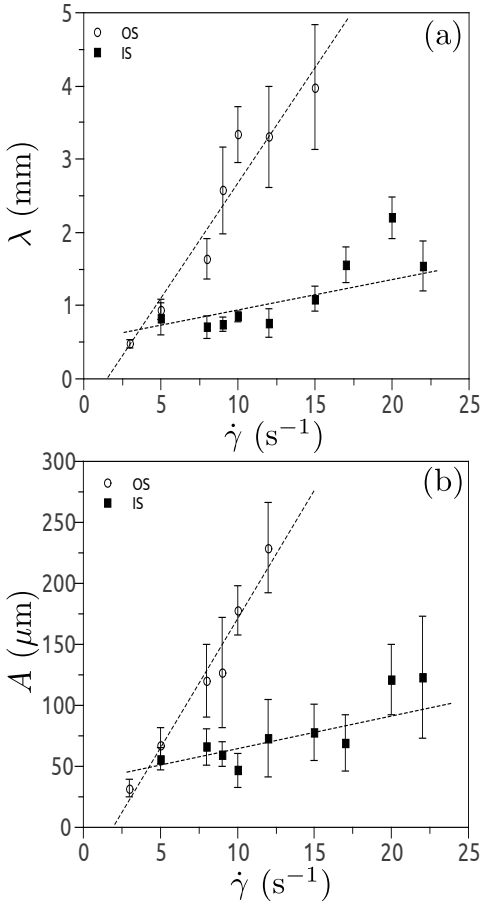

FIG. 5. Asymptotic wavelengths and amplitudes of the interface for the OS (open circles ◯) and IS (black squares ■). (a) Asymptotic wavelength λ versus $\dot{\gamma}$. (b) Crest-to-crest amplitude A of the interface profile as a function of imposed shear rate $\dot{\gamma}$. Dotted lines are guides for the eyes.

For the IS, the destabilization of the interface occurs on shorter time scales in agreement with the stress time series in the inset of Fig 2. Before the regime of turbulent bursts, no spatially stable interfacial pattern is observable. At 3 s^{-1}, the initially growing mode presents a well-defined wavelength ($\lambda \sim 0.3$ mm) but the pattern becomes rapidly disordered with propagative events and vertical oscillations so that no single well-defined wavelength can be defined on long time scales. At higher shear rates, interfacial undulations are clearly visible but the resulting patterns are irregular due to 'continuous' nucleation and relaxation of new crests in the interface profile. We invite the reader to watch the supplementary movies where this peculiar dynamics is unequivocal. Besides, light and dark grey zones in the diagrams tend to oscillate vertically with a small amplitude. These complex dynamics are identical to those observed in the O-OS (see Sup. Fig. 4). Furthermore, interestingly, the spatiotemporal diagram at $\dot{\gamma}$=17 s^{-1} reveals that the system can become locally turbulent away from the edges of the TC device as illustrated by the small white patch that appears around $t \sim 200$ s. This turbulent burst is rapidly damped in time and space but other types of situations are possible as for instance in Sup. Fig. 5 (corresponding to the IS at 20 s^{-1}), which also shows that the turbulent bursts can nucleate anywhere along the height of the TC cell and grow noticeably in time and space before being damped. Propagation of turbulent bursts from a given position along the vorticity direction towards the lower and upper edges of the TC cell have been observed both for the OS and IS. Note that the asymptotic patterns we describe can also be obtained in stress-controlled mode (data not shown).

2. Summary

From the spatio-temporal diagrams shown in Fig. 4, we can extract the wavelength λ and the amplitude A of the interface profile in the 'asymptotic' state. The proportion of the turbid band can also be computed from integration of the position of the interface as a function

of the z-coordinate. For the two samples, the results are in very good agreement with the proportion α_h of the high shear rate band gathered from USV experiments that we will shortly discuss, showing a correspondence between the turbid band observed by 2D visualisation, and the high shear rate band observed by 1D velocimetry (Fig. 12). As for the wavelength and amplitude of the long-time dominant mode (Fig. 5), they are found to increase linearly with $\dot{\gamma}$ for the OS, while the tendency is clearly less marked for the IS, for which λ and A seem roughly constant below the turbulent burst regime, a feature also observed for the O-OS (data not shown).
Hence, despite quantitatively similar global rheological behaviors, the OS and IS (as well as the O-OS) present noticeable differences in their local flow dynamics. The fact that the wavelength and the amplitude of the interface profile and the proportion of the induced band are smaller for the IS at a given applied shear rate suggests that the true shear rate supported by this sample may be lower, for instance because of wall slip. This wall slip may also be responsible for the more disorganised dynamics of the secondary vortex flow before the onset of turbulent bursts.

B. 1D velocimetry–Impact of secondary flows and slip on the main flow

1. *Time-resolved velocity profiles and stress time series*

In order to perform USV, tracers were suspended in the OS and IS. We observe no noticeable influence of the seeding particles on the linear or non-linear rheology, as evidenced by Sup. Fig. 6 and Sup. Fig. 7, which display the linear and non-linear rheology with or without tracers. To study the dynamics of the main flow field at a given $\dot{\gamma}$, we compute the local shear rate $\dot{\gamma}(x/e,t)$ by differentiating the velocity profiles $v(x/e,t)$ recorded at a fixed location in the vorticity direction and gathered in the different regimes of the flow curve for the OS and the IS. Figure 6 displays several spatiotemporal diagrams summarizing the overall flow dynamics along the flow curve for the two samples. The diagrams are coded in linear grey levels with dark regions associated with smaller values of the shear rate.

Even if the temporal resolution is insufficient for an accurate description of the band formation following the start-up of flow, a transient response is observable in almost all of the diagrams. The scenario is similar for all global shear rates $\dot{\gamma}$: the banding structure develops within a few seconds with the interface between the high and low shear bands approximately located at mid-gap. This rapid process is followed by a slow migration of the interface towards the rotor up to a mean position with a characteristic time comparable to the time for the shear stress to reach its 'steady' state. This short-time dynamical response is completely consistent with optical visualization and shear stress time series as discussed in details previously [3, 23]. Thereafter we focus on the longer time scales and specify the features of time-resolved velocity profiles depending on the applied shear rate.

Competition between shear-banding and wall slip at the beginning of the stress plateau?

First, we investigate shear-banding flows at the very beginning of the stress plateau. We recall that from direct optical visualization (Fig. 3 and Fig. 4), for both samples, a tiny turbid band is already present against the moving wall at $\dot{\gamma}$=3 s^{-1}. This observation is fully compatible with the transient shear stress profile in Fig. 2 at the same shear rate, typical of the formation of a banding structure. In contrast, using USV, no banding structure is detected for the IS, while a tiny high shear rate band confined to 1 or 2 pixels is intermittently apparent at the inner wall for the OS. In contrast with Ref. [19], we do not observe nucleation and melting processes where the high shear rate state is formed over short time windows. The optical visualisation enables us to explore the stress plateau deeper than in Ref. [19]. At the very beginning of the stress plateau, the high shear rate band is too thin to be resolved by the USV technique but is unambiguously detected optically. With slip boundary conditions, we observed a shear banding structure all along the stress plateau. We do not exclude a competition between wall slip and shear banding but clearly, wall slip does not dominate shear banding formation, and consequently does not stabilize the bulk flow in our case.

Weak fluctuations uncorrelated with slip for Taylor-like vortex flow along the stress plateau

For imposed shear rates above 3 s^{-1}, and below $\dot{\gamma}_2^{OS} =$ 12 s^{-1} for the OS and $\dot{\gamma}_2^{IS} = 17$ s^{-1} for the IS, we observe a 'classical' scenario with growth of the high shear rate band with increasing $\dot{\gamma}$ and an interface that fluctuates moderately around its steady position. In this range of $\dot{\gamma}$, additional information can be gathered from the analysis of each individual profile. From linear fits performed in each band, we can deduce the low and high shear rates $\dot{\gamma}_l(t)$ and $\dot{\gamma}_h(t)$, the slip velocity $v_s(t)$ at the moving wall and the proportion $\alpha_h(t)$ of the high shear rate band. Note that wall slip at the fixed outer wall is always negligible in this range of shear rates. Fig. 7 compares the evolution of $\sigma(t)$, $v_l(t)$ and $v_h(t)$ (the velocities at two particular positions in the gap chosen in each band), $\dot{\gamma}_l(t)$ and $\dot{\gamma}_h(t)$, $v_s(t)$ and $\alpha_h(t)$. All those quantities nearly follow the same evolution for the two samples. Except for the local velocity $v_l(t)$ and the local shear rate $\dot{\gamma}_l(t)$ that level off more quickly, each quantity settles with approximately the same characteristic time ($\sim$ 100-150 s). However, a quantitative correlation between each of them is far from being obvious. Just after the quench $\dot{\gamma}_l$ and $\dot{\gamma}_h$ start from the same value, emphasizing that the velocity profile is linear at the very beginning. Moreover, slip sets in immediately. The subsequent behavior is associated with the formation and migration of the interface towards its final position : the interface forms during

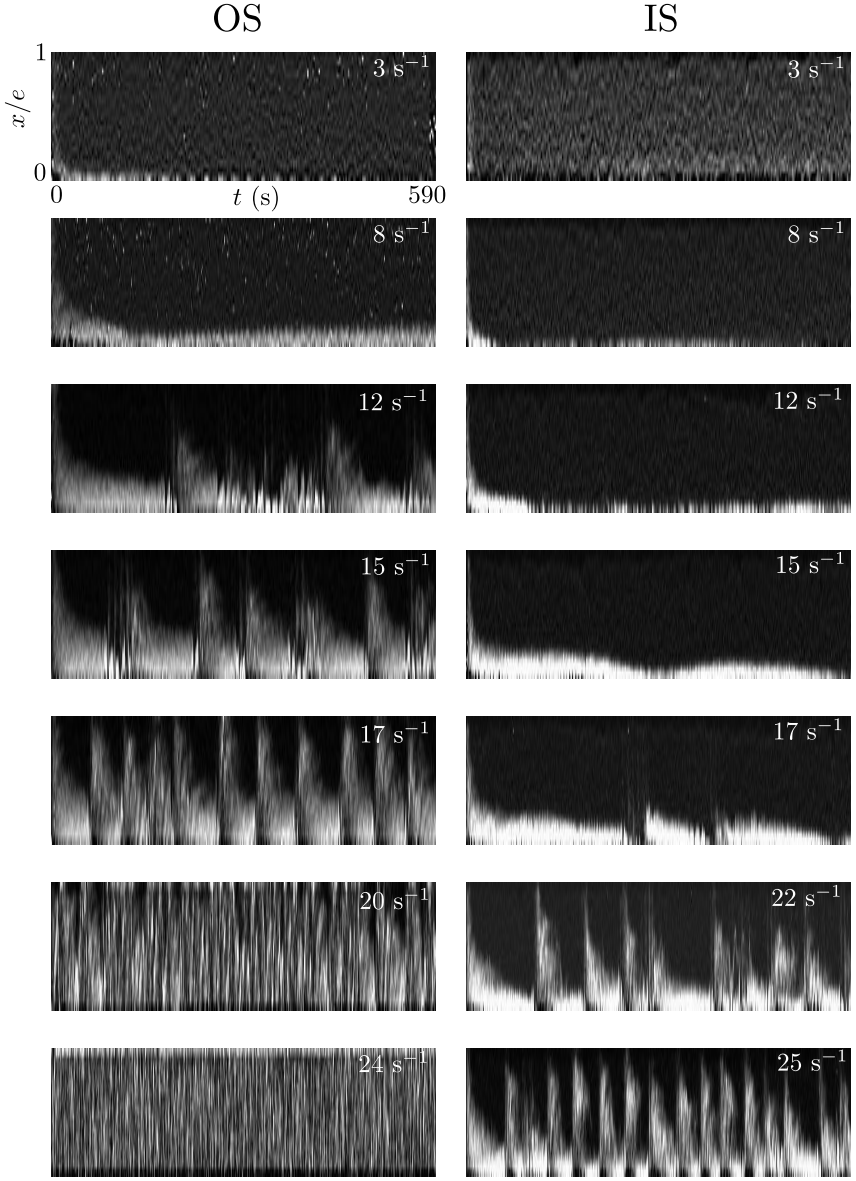

FIG. 6. Spatiotemporal diagram in linear gray scale of the local shear rate $\dot{\gamma}(x/e,t)$ at various applied shear rates $\dot{\gamma}$ covering the flow curve for the OS and IS. Black and white correspond respectively to $\dot{\gamma}(x/e)$=0 s^{-1} and $\dot{\gamma}(x/e)= a\dot{\gamma}$ with a in the order of 2-4 in the explored range of imposed shear rates. The duration of each step shear rate is 590 s and x/e is the dimensionless position in the gap (0 and 1 are associated respectively with the rotor and the stator). The temporal resolution is between 0.5 and 1 s per velocity profile, depending on the global shear rate $\dot{\gamma}$.

the stress overshoot in the bulk of the material [3], since the proportion of the highly sheared material starts at a value $\alpha_h > 0.5$. The decrease of α_h indicates that the interface moves from its initial position towards the rotor. The slow migration process gives rise to an increase of $\dot{\gamma}_h$ while the variation of $\dot{\gamma}_l$ appears subtler, with an abrupt decrease followed by a smooth increase. As for the slip velocity, it globally increases during this process but sometimes exhibits rapid variations ($t \sim 100$ s). Note that such a transient behavior has already been observed on the same system at different concentrations [19, 52]. Finally, once the interface has reached its final position in the gap, all the quantities fluctuate around their mean value. However, the local shear rates exhibit temporal fluctuations, with magnitude between 15 and 25% for $\dot{\gamma}_h$ and between 3 and 10% for $\dot{\gamma}_l$. Those features were already noted in Refs.[19, 20], with either slip or stick boundary conditions. Moreover, as in Ref. [20], no obvious temporal correlation can be established between the local shear rates, the slip velocity, the relative proportions of the bands and the shear stress. Since a direct correlation between fluctuations and wall slip is difficult

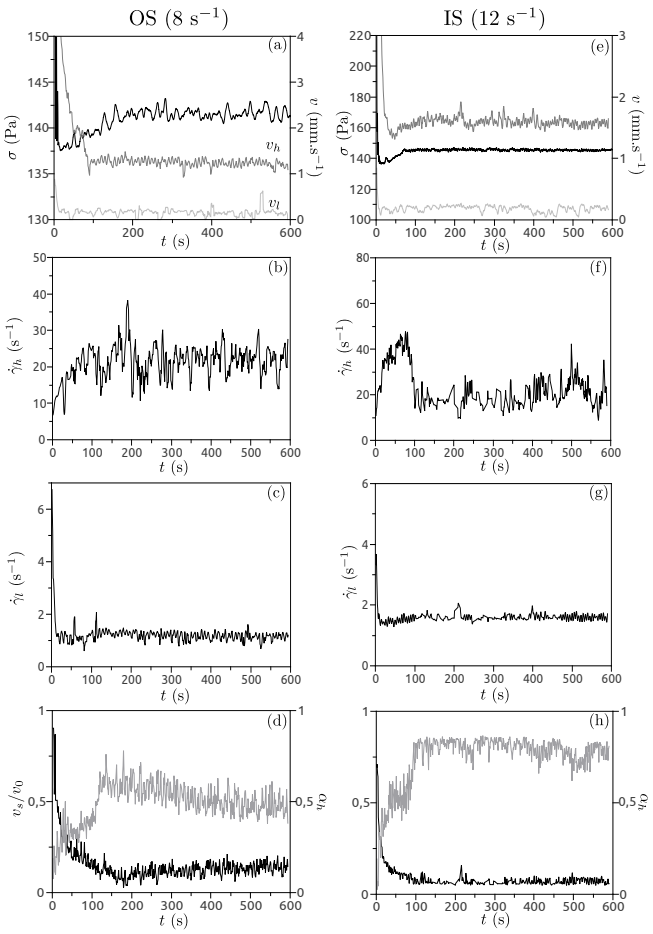

FIG. 7. Analysis of the velocity data at $\dot{\gamma}$=8 s^{-1} for OS and $\dot{\gamma}$=12 s^{-1} for IS. (a) and (e) Comparison between the shear stress σ (black line) and the velocities v_l (light grey line) and v_h (dark grey line) at two specific points in the gap as a function of time. The two particular locations are chosen in the low and high shear rate bands (x/e=0.16 and 0.82 respectively). (b) and (f) Local shear rate $\dot{\gamma}_h$ as a function of time computed from a linear fit of the velocity data in the high shear rate band. (c) and (g) Local shear rate $\dot{\gamma}_l$ as a function of time computed from a linear fit of the velocity data in the low shear rate band. (d) and (h) Dimensionless slip velocity v_s/v_0 (grey line) and proportion of the high shear rate band α_h (black line) as a function of time. v_0 is the rotor velocity.

to establish, the hypothesis of wall slip as the main cause of the fluctuations appears unlikely. Instead, the higher level of fluctuations in the high shear rate band can be explained by the existence of the Taylor-like vortices located in this band.

Strong fluctuations correlated with slip for turbulent bursts at the end of the stress plateau and beyond

For imposed shear rates above 12 s^{-1} for the OS and 17 s^{-1} for the IS, the spatiotemporal diagrams reveal a drastic change in the flow dynamics (Fig. 6). These shear rates correspond to the onset of turbulent bursts, and what we can see in the velocity profiles at a given z along the TC cell axis only reflects the local impact of secondary flows on the main flow. Once the shear-banding structure is established, we observe the development of regions bearing a large shear rate (seen as white patches in the spatiotemporal diagrams) that can spread over a significant part of the gap and occur more and more frequently as the shear rate is raised. They also seem associated with the development of a small unsheared region against the moving wall, which can be distinguished by small black patches at $r \simeq 0$ (Fig. 6, see for instance $\dot{\gamma}$=15 s^{-1} for the OS and $\dot{\gamma}$=22 s^{-1} for the IS). Finally, for the OS, at sufficiently high shear rates, the white patches spread over the whole gap and no particular pattern is visible (see $\dot{\gamma}$=24 s^{-1}). Fig. 8 shows a selection of several velocity profiles recorded during the emergence of the white patches for the OS (17 and 20 s^{-1}) and the IS (22 and 25 s^{-1}). The flow dynamics during these events vary extremely rapidly. We have chosen different times that do not reflect precisely the overall dynamics but which reflect the extreme velocity profiles and illustrate some crucial features. Initially, the velocity profile is divided into two shear bands. As the white patches develop, the individual velocity profiles are significantly modified and adopt a wide variety of shapes.

For the IS at 22 s^{-1} (Fig. 8(c)), the shape of the velocity profiles drastically changes for $0.5 < x/e < 1$. Both the local velocity in this zone and the slip velocity at the rotor exhibit huge variations while the low shear rate region is only slightly affected, suggesting that the banding structure is destabilized due to instability of the high shear rate band. Such a situation has also been observed for the OS at lower values of the control parameter ($12 < \dot{\gamma} < 17$ s^{-1}) and is completely consistent with optical visualisations (see Fig. 3 and Sup. movies). At higher applied shear rates (Fig. 8(a-b) and (d)), huge local velocity fluctuations appear in the initial low shear region and the flow is perturbed over the whole gap. In all cases, the velocity profiles take complex shapes, indicating that the shear-banding flow is strongly disorganized : velocity profiles can be smooth with positive or negative curvature (■, □ in Fig. 8(a)); more or less wide apparently unsheared regions can nucleate either at mid-gap or closer to the inner cylinder (see for instance ▲ in Fig. 8(a-b), □ in Fig. 8(b), ▽ in Fig. 8(d)) and, in this last case, the local velocity can pass through a maximum and can locally be larger than the rotor velocity (see Fig. 8(a-b) and (d)); some profiles can be interpreted as bearing at least three shear bands (△, ⋄ in Fig. 8(b)); local velocities can become negative (⋄ in Fig. 8(b)); finally slip can appear transiently at the fixed outer cylinder (▲ in Fig. 8(a), ∘ in Fig. 8(b)).

Most of these features characterizing individual velocity profiles have been reported previously in a concentrated CTAB/D_2O wormlike micellar system using the same velocimetry technique [58]. In particular, the existence of an unsheared region with local velocity higher

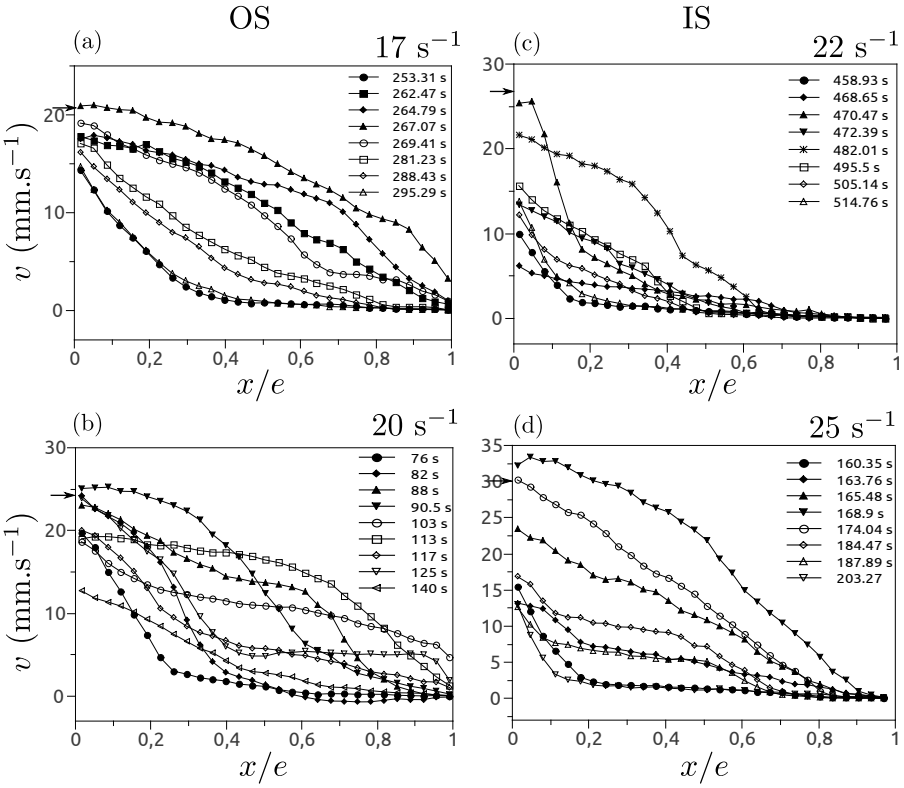

FIG. 8. Selection of several velocity profiles during a turbulent burst for the OS at (a) 17 s^{-1} and (b) 20 s^{-1}, and for the IS at (c) 22 s^{-1} and (d) 25 s^{-1}. The arrow on the left-hand side of each subplot designates the rotor velocity.

than the rotor velocity has been interpreted in terms of three-dimensional instability, taking into account the experimental configuration. Indeed the velocity recorded through USV corresponds to a projection along the acoustic axis and includes contributions from both the radial and azimuthal components of the velocity vector in case of a 3D flow [4, 58]. Note that similar profiles on the same concentrated system have also been observed in Ref. [59] using NMR velocimetry imaging and interpreted in terms of nucleation of a shear-induced 'gel'.
Furthermore, local velocity fluctuations have also been highlighted on the same system as that used in the present study but at a slightly different temperature [18, 39]. The authors demonstrated that, depending on the batch, the CPCl/NaSal 10% system could exhibit either quasi-random or periodic fluctuations. Interestingly, the time-dependent velocity profiles associated with this fluctuating behavior take some shapes reminiscent of those observed in this study (see Fig. 2 in Ref. [18]).

As evidenced by 2D optical visualisation (Fig. 3 and Fig. 4), the fluctuations in the 1D velocity profiles materialized by nucleation and relaxation of white patches in the spatiotemporal diagrams do not correspond to fluctuations of the interface position but rather arise from turbulent bursts that destabilize the high shear rate band, and consequently the banding structure. For the lower applied shear rates in this regime, the dynamics can appear to be intermittent while they become increasingly periodic as $\dot{\gamma}$ is increased. However, the duration of our experiments is clearly not long enough to perform satisfying statistical tests and longer time series are required to make definitive conclusions. This exhaustive study of the statistical properties of the elastic turbulence is left for a future investigation [60].
Fig. 9(a) and (b) give an example of the variations in the σ, v_l, v_h, v_s and α_h time series in the turbulent bursts regime for the OS at 17 s^{-1}. As foreseen in Fig. 8, the local velocities v_l and v_h undergo huge oscillations as a burst develops. These turbulent events happen abruptly : the jump in the local velocities is coupled to an abrupt drop of the slip velocity at the moving inner wall to almost zero and the proportion α_h occupied by the highly sheared material reaches unity, indicating that, at the position along the vorticity axis where the velocity measurements are performed, the turbulent flow invades the whole gap. The relaxation of the bursts is slower, and can extend over several tens of second, depending on $\dot{\gamma}$ as illustrated in Sup. Fig. 3. During this process, the shear-banding structure builds up again and v_l, v_h, v_s and α_h relax towards their mean value associated with the corresponding banding state.
Fig. 9(b) evidently shows a strong correlation between fluctuations of the slip velocity and occurrences of turbulent bursts. Interestingly, the arrival of a turbulent

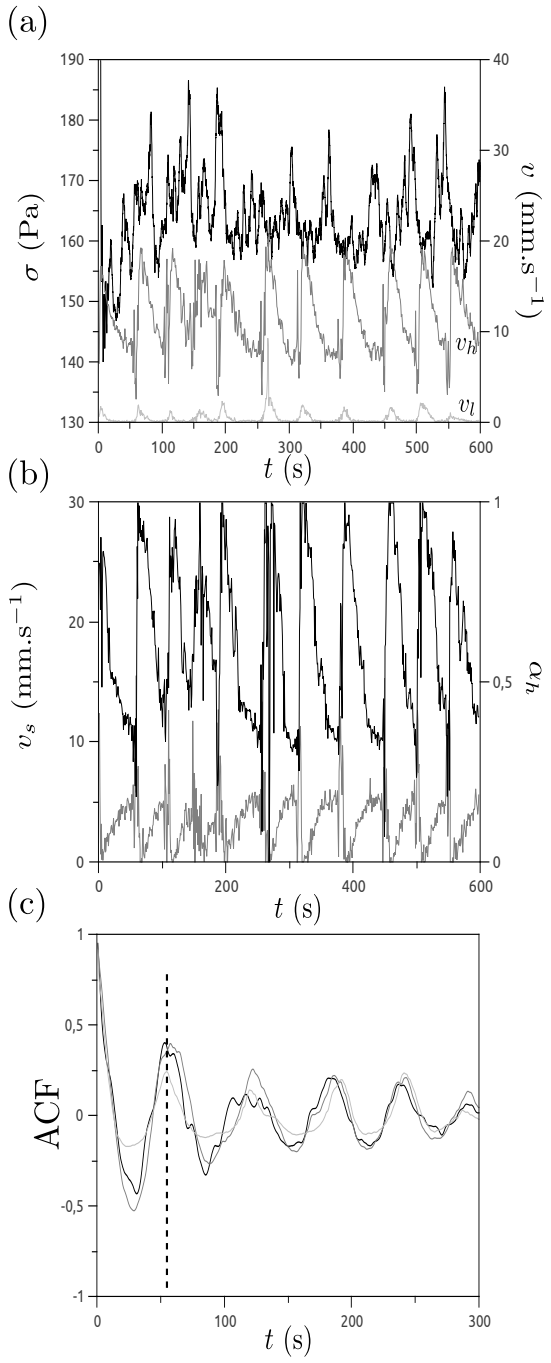

FIG. 9. Analysis of the velocity data at $\dot{\gamma}$=17 s^{-1} for the OS. (a) Comparison between the shear stress σ (black line) and the velocities v_l (light grey line) and v_h (dark grey line) at two specific points in the gap as a function of time. The two particular locations are chosen in the low and high shear rate bands (x/e=0.82 and 0.16 respectively). (b) Slip velocity v_s (grey line) and proportion of the high shear rate band α_h (black line) as a function of time. (c) Autocorrelation function of the $\sigma(t)$ (black line), $v_h(t)$ (dark grey line) and $v_l(t)$ (light grey line) signals. The dotted line indicates the correlation time at $t = 54$ s

burst at the location of the USV measurement seems to decrease wall slip. The stress signal also exhibits huge fluctuations in the turbulent bursts regime. Fig. 9(c) compares the autocorrelation function of the $\sigma(t)$, $v_h(t)$ and $v_l(t)$ time series at $\dot{\gamma} = 17$ s^{-1} for the OS. Remarkably, the global mechanical signal and the local velocity signals present the same characteristic time (~ 54 s at this shear rate). Note that such a coupling between stress, velocity and slip fluctuations has been reported on the same system at a different temperature [18] where the sample was also quenched at a relatively high shear rate in the plateau regime.

Summary

The temporal fluctuations of the 1D velocity profiles at a given location along the vorticity direction reflect the secondary flows that can be directly imaged using visualization. For $\dot{\gamma} < \dot{\gamma}_2$, 2D visualisation shows interfacial instability and 3D vortex flow, while the 1D velocity profiles exhibit no significant signature, except greater fluctuations in $\dot{\gamma}_h$ with respect to $\dot{\gamma}_l$. Local velocities larger than the rotor velocity were not observed and the velocity profiles adopt a classical shape with coexistence of two well-defined shear bands. Particle image velocimetry measurements have provided estimates of the radial velocity component of the 3D vortex flow to be between two and three orders of magnitude lower than the base azimuthal velocity [24]. This may explain why no radial velocity contribution is detected in the USV experiments. At larger shear rates on the plateau, turbulent bursts emerge, creating strong fluctuations when they pass the location where USV measurements are performed. In

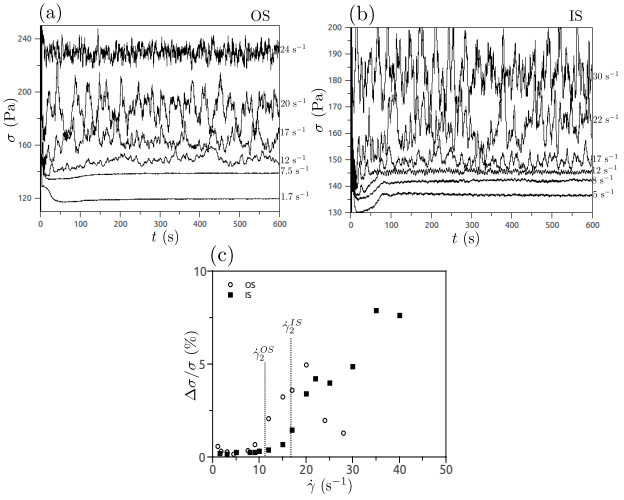

FIG. 10. Shear stress time series for various applied shear rates along the flow curve : (a) OS and (b) IS. The corresponding values of the shear rates are indicated at the right hand side of the plots. (c) Shear stress fluctuations as a function of the applied shear rate for the OS (open circles) and the IS (closed squares).

this regime, the fluctuations are very strong, they couple with wall slip, and 3D velocity components can be captured by velocimetry, as in Ref. [58].

Overall, the shear stress time series are a good and readily attainable estimate of the type of secondary flow regime. Fig. 10(a) and (b) display the shear stress time series for various applied shear rates $\dot{\gamma}$ greater than $\dot{\gamma}_1$. The magnitude of the fluctuations is low and nearly constant at the beginning of the plateau ($\Delta\sigma/\sigma$ ∼0.2-0.5%), when secondary flows are coherent. Note that the growth of the secondary flows is observable in the global rheology through the undershoot in the transient shear stress [23, 24]. Fluctuations begin to grow significantly when $\dot{\gamma}_2$ is approached, *i.e.* at the onset of turbulent bursts. The magnitude of the fluctuations reaches 5% for the OS around 20 s^{-1} and 7% for the IS around 35 s^{-1} before decreasing [see Fig. 10(c)]. The increase in the amplitude of the fluctuation level corresponds to more frequent turbulent bursts, whereas the subsequent decrease of fluctuations reflects the state of (more) homogeneous turbulence, a characteristic signature of subcritical transitions [25]. Note that for the IS, shear rates high enough for the turbulent state to become homogeneous could not be reached before instability of the free surface. Therefore a clear decrease in the amplitude of fluctuations could not be reached in the IS.

Note that the temporal fluctuations of the controlled shear rate never exceed 0.05%. Such shear stress time series with huge fluctuations have already been reported on this system at the same concentration in Refs. [18, 39]. The analysis of the fluctuations using power spectrum and autocorrelation indicates that characteristic times, ranging typically between 25-100 s, can be identified in the mechanical signals beyond 13 s^{-1} for the OS and 22 s^{-1} for the IS.

2. *Time-averaged velocity profiles and the lever rule*

The plots (a) to (f) in Fig. 11 display the time-averaged velocity profiles recorded at a fixed location in the vorticity direction and gathered in the different regimes of the flow curve for the OS and the IS. For applied shear rates below 12 and 17 s^{-1} respectively for the OS and IS (*i.e.* for $\dot{\gamma} \lesssim \dot{\gamma}_2$), individual velocity profiles are averaged over 200 s discarding the early times. For larger shear rates, turbulent bursts occur and averages are computed over 30 to 60 s, in between bursts.

The error bars, which correspond to standard deviation of the local velocity, point out that, in both cases, the local flow field is strongly fluctuating. The amplitude of the fluctuations appears much larger when the turbulent burst start, and the shape of the average velocity profiles radically changes when the applied shear rate is further increased ((c) and (f)), reflecting the fact that the banding structure can not be fully recovered when the turbulent bursts become too frequent, or simply disappears when the turbulence becomes 'homogeneous' (*i.e.* not intermittent any more). Also noticeable is the increased apparent wall slip at the inner wall. The average velocity profiles become smoother and display a significant curvature for the IS (see $\dot{\gamma} = 25$ and 35 s^{-1}) while an almost linear variation is observed for the OS (see $\dot{\gamma} = 20$ and 28 s^{-1}). In this last case, we observe a small unsheared region against the moving wall and significant slip at the fixed outer cylinder.

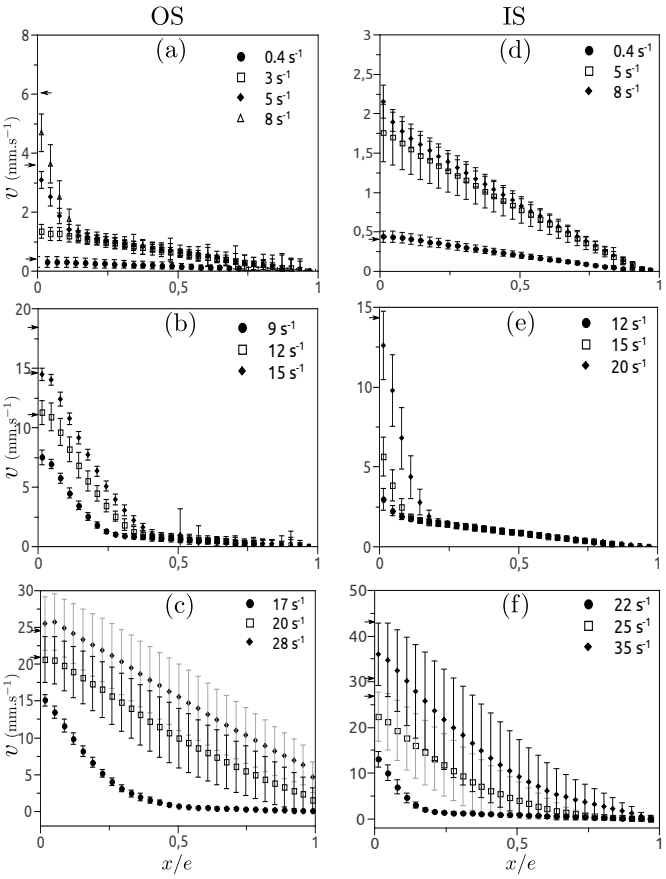

FIG. 11. Time-averaged velocity profiles at different applied shear rates along the flow curve for the OS (a-b-c) and the IS (d-e-f). The time interval between each velocity profile is between 0.5 and 1 s depending on the applied shear rate. The average is taken over the last 200 s of the time resolved velocity profiles shown in Fig. 6, except for the highest applied shear rates ((c) and (d)) for which the average is computed over 30-60 s (in between turbulent bursts whenever possible). The errors bars represent the standard deviation on the mean estimate. The dimensionless positions of the outer and inner cylinders are respectively 0 and 1. Arrows on the left side of each figure represent, if the scale makes it possible, the imposed velocity of the inner rotating cylinder.

From the averaged profiles, we can compute the mean values of $\dot{\gamma}_l$, $\dot{\gamma}_h$, v_s and α_h. The variation with imposed shear rate $\dot{\gamma}$ of the mean values of $\dot{\gamma}_l$, $\dot{\gamma}_h$, v_s and α_h is given in Fig. 12 and appears qualitatively similar for the OS and the IS. Below 1.2-1.5 s^{-1}, *i.e* below $\dot{\gamma}_1$ on the flow curve, slip is absent and the local shear rate

coincides with the applied shear rate (see Fig. 11(a)). Above $\dot{\gamma}_1$, as the high shear rate band develops, slip at the moving wall appears and increases noticeably with $\dot{\gamma}$, suggesting that slip results from specific interactions between the shear-induced structures and the wall. Whatever the applied shear rate above $\dot{\gamma}_1$, the development of the high shear rate band is accompanied by slip at the inner wall, in agreement with a recent observation on the same system flowing in a TC cell with smooth boundary conditions [19]. Note that slip preceding shear-banding formation in the same system has also been reported both in rough and smooth boundary conditions [20].

Moreover, $\dot{\gamma}_l$ remains essentially constant throughout the stress plateau while $\dot{\gamma}_h$ is an increasing function of $\dot{\gamma}$ until it levels off around 12 s^{-1} for the OS and 17 s^{-1} for the IS, namely, when turbulent bursts start to develop. The proportion of the high shear rate band, it increases almost linearly with $\dot{\gamma}$ (for the OS, α_h presents a jump and is close to 1 beyond 20 s^{-1} since the whole gap is filled with the turbulent turbid 'phase' and the 1D mean velocity profile does not show inhomogeneous flow anymore). The variations of the shear rate $\dot{\gamma}_h$ is also coupled to a non trivial variation of the slip velocity that increases almost linearly for the two samples then saturates when approaching the turbulent burst regime. Standard deviations of v_s become significantly larger in this regime, suggesting that the bulk rheology is affected by the walls. Several recent experimental studies have reported this type of anomalous behaviour in various semi-dilute and concentrated micellar solutions [20, 58, 62–64]. Nonetheless the precise meaning of 'anomalous' can vary from study to study, and we will discuss this point further in section IV.

Despite qualitative similarities, the two samples present some quantitative differences. The magnitude of slip at the moving wall rapidly becomes much larger for the IS, implying a smaller true shear rate supported by the IS. Consequently, at a given applied shear rate, the proportion of the high shear rate band is much smaller for the IS, a feature foreseen through the optical visualisations. Finally, although the value $\dot{\gamma}_l$ remains similar for both samples and in agreement with $\dot{\gamma}_1$ inferred from the flow curve, a strong departure is observed for $\dot{\gamma}_h$ that can reached 30 and 50 s^{-1} for OS and IS respectively, whereas $\dot{\gamma}_2$ had been estimated to be 12 and 17 s^{-1}.

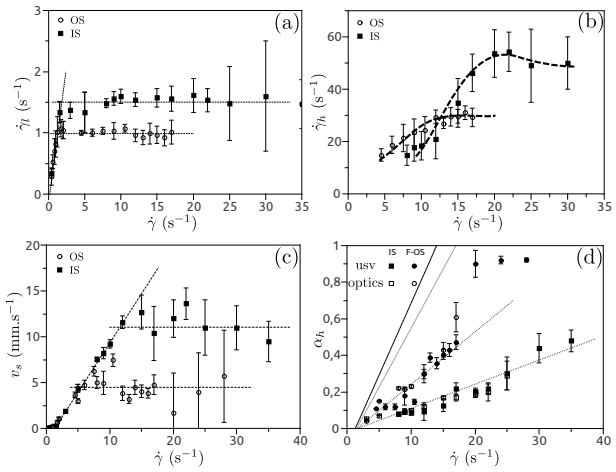

FIG. 12. Mean asymptotic values of (a) $\dot{\gamma}_l$, (b) $\dot{\gamma}_h$, (c) v_s and (d) α_h, as a function of imposed shear rate $\dot{\gamma}$. The error bars represent standard deviations on the estimate of the mean value. In subplots (a) to (c), the open and closed symbols correspond respectively to the OS and the IS and dotted and dashed lines are guides for the eyes. In subplot (d), circles and squares differentiate between the OS and the IS. Closed and open symbols compare the proportion of highly sheared material gathered from USV experiments and optical visualisations respectively. The black and gray dashed lines represent standard lever rule predictions respectively for the OS and IS computed using $\dot{\gamma}_1$ and $\dot{\gamma}_2$ extracted from the corresponding flow curves. Dotted lines are linear fits of $\alpha_h(\dot{\gamma})$.

IV. DISCUSSION

The high shear rate band and the turbid band following the onset of shear-banding show quantitatively the same evolution of their proportion as a function of the applied shear rate. The velocimetry and optics experiments are performed in the same flow geometry and this demonstrates that turbidity and shear bands are closely related. In the following, we do not regard this point as controversial [65]. Note that such a correlation had been previously reported on the same system at other concentrations [64]. Obviously, we do not reject the possibility of shear-banding systems with no noticeable turbidity contrast, but in semi-dilute micellar systems, they are most likely the exception rather than the rule.

A. Systematic wall slip and the lever rule

In the introduction, we mentioned the 'simple lever rule' given by the following equation:

$$\dot{\gamma} = (1 - \alpha_h)\dot{\gamma}_1 + \alpha_h\dot{\gamma}_2 \qquad (1)$$

In the classical shear-banding scenario [61], this equation results from the fact that the global shear rate $\dot{\gamma}$ should correspond to the integration of the shear rate profile across the gap. If the shear rate profile is a step function separating the high and low shear rate bands respectively with proportions α_h and $\alpha_l = 1 - \alpha_h$, and shear rates $\dot{\gamma}_2$ and $\dot{\gamma}_1$, one trivially recovers Eq. (1). One can also picture a velocity profile made of two segments without wall slip and recover Eq. (1) by trigonometry. In the classical shear-banding scenario [61], the shear rates $\dot{\gamma}_1$ and $\dot{\gamma}_2$ are assumed to be constant for a given sample, and to take the values given by the boundaries of the stress plateau on the flow curve. But the flow curve to consider must be the *true* flow curve. If $\dot{\gamma}_1$ and $\dot{\gamma}_2$ are

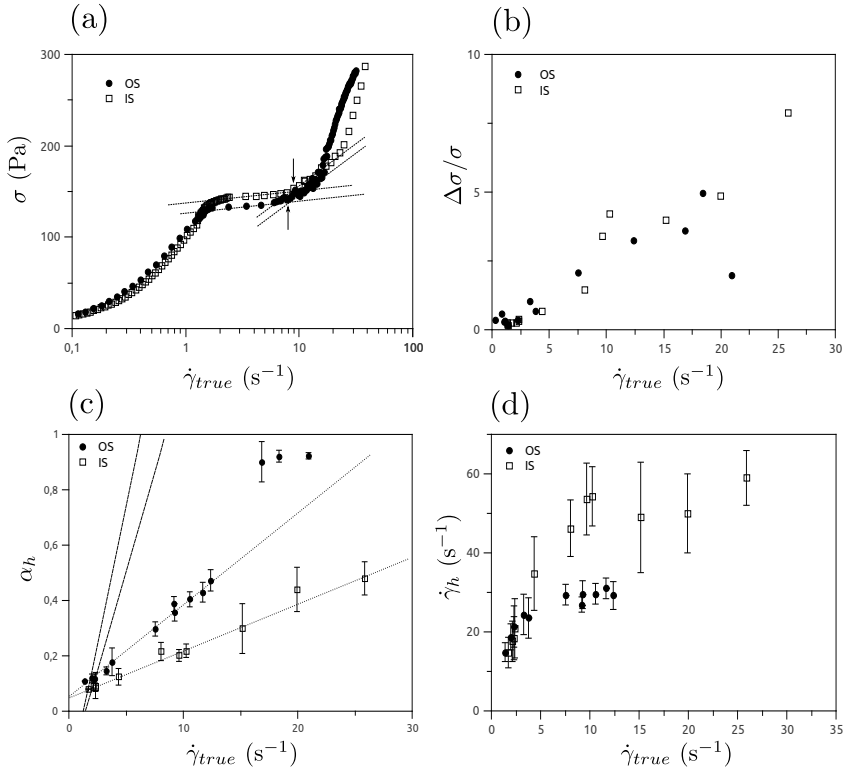

FIG. 13. (a) Apparent flow curves replotted as a function of the true shear rate $\dot{\gamma}_{true} = |v(0) - v(e)|/e$ for the OS (•) and the IS(□). (b) Shear stress fluctuations *versus* $\dot{\gamma}_{true}$ for the OS (•) and the IS(□). (c) Proportion α_h as a function of $\dot{\gamma}_{true}$. The dashed lines correspond to the prediction of the simple lever rule when slip effects are subtracted (Eq. 1), *i.e.* using as the local high shear rates $\dot{\gamma}_2$, the values of $\dot{\gamma}_{true}$ designated by the arrows in the subplot (a) (6.3 and 8.4 s^{-1} for OS and IS respectively). The dotted lines are linear fits. (d) Local shear rate $\dot{\gamma}_h$ in the high shear rate band as a function of $\dot{\gamma}_{true}$.

instead taken from the *apparent* flow curve, a disagreement between the predictions of the simple lever rule and the data must be expected, especially in the presence of wall slip, if the flow curve has been measured in curved geometry or if secondary flows are present. Predictions of such *naive simple lever rule* are drawn in subplot (d) of Fig. 12 for the two samples (dotted lines), clearly showing no agreement with the data. This poor prediction should not really be seen as a genuine abnormal behavior, since it can only be due to the fact that the apparent and true flow curves are different.

In our experiments, the effects of curvature on the flow curve are expected to be small, due to the small gap ratio of the geometry. Moreover, before the onset of turbulent bursts, secondary flows do not seem to modify the evolution of the proportion of high shear band too dramatically (Fig. 12). Therefore, for $\dot{\gamma} < \dot{\gamma}_2$, we can discuss the lever rule behavior we observed as being influenced principally by wall slip. Our data and previous studies [58, 62–64] suggest three important points that can help to construct an appropriate lever rule beyond the *simple lever rule*.

1. First, the value of shear rate corresponding to the beginning of the plateau of the apparent flow curve is a good estimate of the local value of shear rate in the low shear rate band, all across the shear-banding regime (except of course when secondary flows become turbulent). This means that the shear rate in the low shear rate band is essentially constant and $\dot{\gamma}_l = \dot{\gamma}_1$, for all $\dot{\gamma}$ on the plateau (Fig. 12(a)). Moreover, except during turbulent bursts, there is essentially no wall slip on the low shear rate band, *i.e.* $v(e) \simeq 0$. This was already the case in the simple lever rule.

2. Second, the proportion of high shear rate band α_h increases linearly with the global shear rate. In Fig. 12(d), linear fits of $\alpha_h(\dot{\gamma})$ ignoring the influence of turbulent bursts and their extrapolations to $\alpha_h = 1$ lead to $\dot{\gamma}_2^* = 37$ and 78 s^{-1} respectively for the OS and IS. These could provide reasonable estimates for the upper limits of the true stress plateau in the absence of turbulent bursts. However, wall slip has still to be taken into account. Therefore in Fig. 13(c), the global evolution of α_h is plotted as a function of the true shear rate $\dot{\gamma}_{true}$, defined as $\dot{\gamma}_{true} = |v(0) - v(e)|/e$. The proportion of high shear rate band α_h vs $\dot{\gamma}_{true}$remains far from the prediction of the simple lever rule, and a linear regression with $\alpha_h = 0$ at the beginning of the stress plateau no longer fits the data. The evolution of α_h with $\dot{\gamma}_h$ rather seems sublinear, which is indicative of a more subtle dependence of α_h on the applied shear rate and on wall slip.

3. Third, and this is the noticeable departure from the simple lever rule, the shear rate in the high shear rate band is not constant. Its value increases with the global shear rate $\dot{\gamma}$ and then levels off, as evidenced in Fig. 12(b) for the two samples. The same trend is observed if $\dot{\gamma}_h$ is plotted against the true shear rate $\dot{\gamma}_{true}$, as seen in Fig. 13(d).

The dependency of the local high shear rate on the global shear rate $\dot{\gamma}_h(\dot{\gamma})$ (*3*) was defined recently as the salient feature of what was called an *anomalous lever rule* [20]. In ref. [20], the authors argued that anomalous lever rule behaviors have been found when the applied shear rate is incremented in small steps. They postulated that establishment of a shear-banding structure with a constant $\dot{\gamma}_h$ corresponding to the upper limit of the (true) stress plateau could be achieved through quench experiments, the magnitude and duration of the stress overshoot being sufficient to nucleate the alignment state of the wormlike micelles corresponding to a constant $\dot{\gamma}_h$. Our observations using quench experiments demonstrate that no shear pre-history is needed to generate violation of the simple lever rule.

When point *3* is observed in conjunction with point *1* and *2*, we shall say that we have a *standard anomalous lever rule*, which indeed seems to be widespread across systems [58, 62–64]. However, very recently, Feindel et al. [20] also described a *pathological anomalous lever rule* behavior for the CPCl 10% system. In their experiments, the relative proportion of each band remained essentially constant with $\dot{\gamma}$ while the local shear rates $\dot{\gamma}_l$ and $\dot{\gamma}_h$ varied : $\dot{\gamma}_l$ rose in a small range of $\dot{\gamma}$ before staying constant and $\dot{\gamma}_h$ increased almost linearly before showing erratic fluctuations. In our experiments, no such pathological behavior is observed. Note nonetheless, that the pathological behavior of ref. [20] might have been due to impurities in the sample. Experiments on the IS show that UV-light exposure itself can generate impurities (products of photochemical reactions detailed in the ESI), which in particular generate an enhanced wall slip and a proportion of induced band α_h growing very slowly with the applied shear rate. Note that if the plot of $\alpha_h(\dot{\gamma})$ for the IS in Fig. 12(d) is restricted to shear rates lower than 15 s^{-1}, which corresponds to the maximum investigated in Feindel *et al.* [20], the proportion α_h in the IS could somewhat rushingly be interpreted to be constant.

Let us discuss the behavior one would expect if the wall slip of the high shear rate band satisfies the mixed boundary condition given by Navier's slip law [66, 67]:

$$v_s = b\dot{\gamma}_h \tag{2}$$

With $b \equiv \beta_h e$ the (intrinsic) *slip length* on the high shear rate band. The length b is also called the 'extrapolation length', because it is the length, for $x < 0$, necessary for the velocity profile given by $\dot{\gamma}_h$ to reach the value of the velocity of the wall v_0 (not 'at' the wall, which we recall was $v(0)$ obtained by USV).

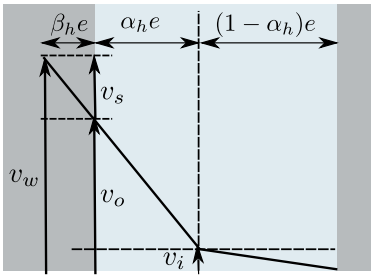

FIG. 14. Sketch of a shear-banding flow with wall slip on the high shear rate band.

If we neglect the curvature of the TC cell, $v_0 = \dot{\gamma}e$, and we can obtain a modification of the simple lever rule taking into account the three points *(1-3)* summarizing our observations. The typical flow we are describing is sketched in Fig. 14.

If the flow geometry has no curvature, we have a simple relation between the true shear rate and the slip shear rate $\dot{\gamma}_s \equiv v_s/e = \dot{\gamma} - \dot{\gamma}_{true}$. Navier's slip law is then expressed by the following equation:

$$\dot{\gamma}_h = \frac{\dot{\gamma}_s}{\beta_h} = \frac{\dot{\gamma} - \dot{\gamma}_{true}}{\beta_h} \tag{3}$$

From Eq. (2) or Eq. (3), we can estimate the value of β_h across the stress plateau for the OS and IS. The propagation of errors from v_s and $\dot{\gamma}_h$ only allows for the rough estimate that $\beta_h^{OS} = 0.2 \pm 0.1$ and $\beta_h^{IS} = 0.3 \pm 0.1$, across the shear-banding regime. We can finally express a *Navier lever rule* in two equivalent forms:

$$\begin{cases} \dot{\gamma} = (1-\alpha_h)\dot{\gamma}_l + (\alpha_h + \beta_h)\dot{\gamma}_h \\ \dot{\gamma}_{true} = (1-\alpha_h)\dot{\gamma}_l + \alpha_h\dot{\gamma}_h \end{cases} \tag{4}$$

The two above equations take forms similar to the simple lever rule. When the lever rule is expressed as a function of the global shear rate, it depends explicitly on the slip length through β_h. If the true shear rate is used instead of the global shear rate, the explicit dependency on the slip length disappears. The limits between the different regimes in the global rheology of the OS and IS samples become smaller [Fig. 13(a)], and the shear stress fluctuations appear similar for both samples [Fig. 13(b)]. Replacing the global shear rate by the true shear rate allows for a better collapse of the data from the OS and IS, but it does not subtract all the effects of wall slip. It is capital to remember that the Navier lever rule is anomalous whenever $\dot{\gamma}_h$ is a function of $\dot{\gamma}$ or $\dot{\gamma}_{true}$. The fact that the variations of $\dot{\gamma}_h$ and v_s across the stress plateau are similar can be roughly explained by a Navier slip law on the high shear rate band. But the particular dependence of $\dot{\gamma}_h$ on the global or true shear rate is still enigmatic. Note that if the interface between bands is not perfectly sharp, *i.e.* if the shear rate profile is not a step function, systematic wall slip and a high shear rate $\dot{\gamma}_h$ function of

the global shear rate are features that were recently understood to be inevitable in shear-banding flows, and to be connected to stress diffusion [68].

B. Elastic instability of the high shear band triggers secondary flows–The main origin of fluctuations

The main difference between the OS and IS dynamics seems to be an enhanced wall slip in the IS, delaying the onset of turbulent bursts to larger global shear rates and strongly perturbing the dynamics of coherent secondary flows. However, we have seen that both in the OS and IS, fluctuations mainly come from the presence of secondary flows, which break the invariance of the flow along the vorticity axis. Note that the existence of little structures along the vorticity axis had been advanced in Ref. [20], but our set-up allows for a much clearer characterisation (This study was restricted to the begining of the stress plateau, where the amplitude of the pattern does not exceed 120 μm [Fig. 5.b] making detection by the NMR set-up impossible). First Taylor-like vortices generate weak fluctuations, and then, as the global shear rate is increased, turbulent bursts onset and become increasingly frequent, generating very large fluctuations that can locally disrupt the banding structure and couple with wall slip. Eventually, the flow becomes fully turbulent and bands disappear. Both USV and optics measurements clearly show that this succession of complex flow states comes from an instability of the high shear rate band. This phenomenology is not completely identical to the one exposed in details about the CTAB/$NaNO_3$ system [22–25], but we will show here that it can still very well be explained by invoking the mechanism of bulk elastic instability of the induced (turbid/high shear-rate) band.

Let us recall that elastic instabilities are driven by nonlinearities in the constitutive relation [29], the magnitude of which are controlled by the Weissenberg number ($Wi = \dot{\gamma}\tau_R$). For polymer solutions flowing in curved geometries, a bulk elastic instability can arise above a threshold that follows a general criterion established by Pakdel and McKinley [69]. For purely elastic instability in polymers, the flow becomes unstable as the dimensionless number $\Sigma_0 = \sqrt{e/R_i}Wi$ is typically greater that unity [55, 69]. Recently, we extended this criterion to elastic instability in shear banded flows, modelled for instance by the diffusive Johnson-Segalman (dJS) model [53]. We found that the relevant dimensionless group for elastic instability in shear-banding flows is $\Sigma = \sqrt{\alpha_h e/R_i}Wi_h f(\eta)$, where Wi_h designates the local Weissenberg number in the high shear rate band and $f(\eta)$ is a function of the viscosity ratio between the high and low sheared materials, which can be safely assumed to be of order 1 [53]. Using velocimetry data, we can directly compute the values of Σ. Fig. 15 displays the plot of Σ as a function of the global shear rate $\dot{\gamma}$ or true shear rate $\dot{\gamma}_{true}$ in the small gap approximation.

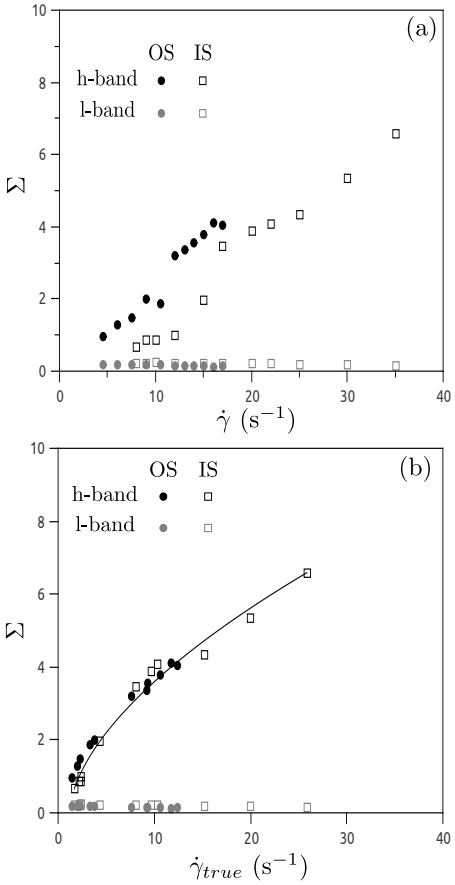

FIG. 15. Instability criterion $\Sigma = \sqrt{\alpha_h e/R_i}Wi_h$ computed for the OS (•) and IS (□) as a function of (a) the global shear rate $\dot{\gamma}$ and (b) the true shear rate $\dot{\gamma}_{true}$. For comparison, results for similar calculation with the low shear band parameters has been added (grey symbols). The solid line in (b) shows the best power-law fit of the data for OS and IS: $\Sigma = A(\dot{\gamma}_{true} - \dot{\gamma}^1_{true})^\delta$, with $A = 1.3$, $\dot{\gamma}^1_{true} = 1.5$ and $\delta = 0.49 \pm 0.05$.

For all the applied shear rates above $\dot{\gamma}_1$ the values of Σ are larger than 1. These values are probably still underestimated since we have used the relaxation time τ_R extracted from the linear rheology. Indeed, the characteristic time scales of the induced phase are usually greater [70]. In contrast, a similar criterion computed from the local parameters characterizing the low shear rate band never exceeds 0.2. Note however that Σ is close to unity at the very beginning of the stress plateau. In this region, where the size of the induced band is small, interfacial modes may predominate [31, 32, 53].

Moreover, if the lever rule was simple and not anomalous, one would expect $\Sigma \sim \dot{\gamma}^{1/2}$, since the only dependence on $\dot{\gamma}$ would come from $\sqrt{\alpha_h}$. Fig. 15(a) clearly shows that this is not the case in our experiments where the lever rule is anomalous and $\dot{\gamma}_h$ brings an additional growing function of $\dot{\gamma}$. When Σ is plotted against the true shear rate $\dot{\gamma}_{true}$, the values of the instability criterion for the

OS and IS nicely collapse onto a single curve which is well fitted by a power law $\Sigma \sim \dot{\gamma}_{true}^{\delta}$ with an exponent $\delta = 0.49 \pm 0.05$. The fact that this exponent is close to 0.5 is most probably fortuitous since it results from a combination of the sub-linear behaviour of α_h and of the increasing behaviour of $\dot{\gamma}_h$ with $\dot{\gamma}_{true}$. At this stage, the remarkable collapse of the instability criteria for both samples on the same power law remains largely unexplained and calls for more investigations.

Let us now discuss the differences between the succession of elastic instabilities observed in this paper and the one observed for the CTAB/$NaNO_3$ system [24, 25]. In the case of the CTAB/$NaNO_3$ system, at respective concentrations 0.3M/0.4M and at T=28°C, the 3D shear-banded vortex flow was confined on the stress plateau, and the transition toward elastic turbulence arose only along the upper branch of the flow curve, as the gap of the TC cell was fully invaded by the induced state and the base flow was homogeneous [25]. A small range of shear rate, beyond the stress plateau and before the onset of turbulence, corresponded to a homogeneous and 1D annular laminar flow. Here, with the 10% CPCl system at T=21.5°C, as the applied shear rate is further increased in the plateau region, the 3D shear-banded vortex flow is destabilized, as illustrated by the regime of turbulent bursts. The system undergoes a transition towards elastic turbulence before reaching the *true* end of the plateau, *i.e.* before $\alpha_h = 1$.

Why does the CTAB/$NaNO_3$ system exhibits a stable range of shear rate beyond the shear-banding regime, whereas the CPCl/NaSal system goes turbulent before the end of the shear-banding regime? In the recent paper where we derived the criterion for elastic instability in shear-banding flows [53], we gave a rationale for such discrepancy. In short, it has to do with the fact that the threshold for the onset of elastic instability, and the type of excited modes depend on the boundary conditions. The threshold for soft BC is smaller than for hard BC $\Sigma_c^s < \Sigma_c^h$ [25, 53], and more modes are usually unstable for hard BC than for soft BC. During shear-banding, the interface with the low shear rate band acts as a soft BC, while beyond shear-banding, when $\alpha_h = 1$, the BC is switched to the hard type. In the CTAB system, we have $\Sigma(\alpha_h = 1) < \Sigma_c^h$, whereas in the CPCl system, we have $\Sigma(\alpha_h = 1) > \Sigma_c^h$. The CTAB and CPCl systems respectively correspond to category 2 and 3 of unstable shear-banding flows discussed in Ref. [53]. Category 1 corresponds to a stable shear-banding flow, *i.e.* when $\Sigma < \Sigma_c^s$ everywhere on the plateau, and is still to be evidenced precisely in experiments.

Note also that in the CTAB system, the onset of turbulence after a laminar 1D flow regime beyond shear-banding was the first instability for a homogeneous flow of micelles with hard BC. Here, the onset of turbulence bursts seem to be a secondary instability for a shear-banded vortex base flow. Note that primary flow instabilities in TC cell in the form of coherent vortex flows subsequently followed by turbulence at higher values of the control parameter is a fairly standard scenario of transition toward chaos [29]. Interestingly, a recent study in a micellar system made of CTAT also reports the observation of a vortex flow followed by turbulent bursts and eventually homogeneous turbulence [28]. Nonetheless, it remains unclear whether shear bands are present or not in this system [71–73].

V. CONCLUSION

In this study, we have used both global and local techniques to explore the shear-banding flow of a surfactant system that is the subject of an abundant literature. The key point and one of the main originality was to use a single Taylor-Couette flow geometry, enabling precise correlation between the different measurements. Large variability has been previously reported in this system, attributed to impurities that vary from one batch to the other, but without suggestion of associated mechanisms at molecular or mesoscopic scales. Here we showed that ambient light exposures could induce modifications in the sample, leading to noticeable changes in the flow dynamics despite very similar global rheological responses. Beyond this variability, from our results and in the context of the recent literature, robust features emerge : the shear-banding flow of the 10% CPCl/NaSal brine system is unstable, at least with respect to perturbations along the vorticity direction, due to elastic instability of the high shear rate band. Wall slip has undoubtedly an impact on the shear-banding flow but fluctuations reported on this system are mainly due to the existence of the 3D (coherent then turbulent) flow resulting from successive instabilities undergone by the high shear rate band. We believe that this phenomenology, also common to the CPCl/NaSal/brine 6% and the CTAB/$NaNO_3$ systems [23] could be shared by other surfactant systems for which fluctuations and unstable flows have been reported [4]. For a given surfactant system, experiments show that increasing the surfactant concentration, or decreasing the temperature tends to increase the value of Wi_h, making thus the flow more unstable, since $\Sigma \sim Wi_h$ [53]. This may explain the larger fluctuations observed by Lettinga *et al.* in the 10% CPCl/NaSal solution in comparison with the 6% CPCl/NaSal solution [19]. A similar remark may also hold for the concentrated CTAB/D_2O solutions investigated by Bécu *et al.* [58, 74], which exhibited huge fluctuations in the velocity profiles [58] that are not observed at higher temperature [74].

In general, in any shear-banding flow of a sufficiently entangled micellar system, there is a clear possibility for secondary flows triggered by elastic instabilities. Global rheology and 1D measurements should therefore be performed with great care. This care should not be restricted to flows in the Taylor-Couette geometry. A very recent study also found evidence for secondary flows potentially triggered by elastic instabilities in the cone-and-

plate flow of a 4.5% CPCl/NaSal solution at lower concentrations [75]. Our data also call for 3D velocimetry experiments to fully resolve the 3D structure of the flow, and a precise control of the surface roughness to better quantify slip effects. Furthermore, the origin of the turbidity and the precise mesoscopic structure of the induced high shear rate band are still open questions.

Finally, let us come back to the O-OS, the abnormal behaviour of which had initially motivated this investigation. The global rheology of this sample conforms to the one of the OS while its flow dynamics strongly differs. The stark contrast between the proportion of the induced band between the OS and O-OS led us to the hypothesis that the interaction with the walls could play a major role in this difference, meaning that alteration at molecular scale, not easily quantifiable through linear rheological measurements, was involved. Photochemical kinetics gathered in the ESI indeed confirmed that the photohydratation of pyridine can occur when the pyridine ring forms the head of a surfactant. Since the micellar mesoscopic structure or the presence of chloride ions prevent the reversibility of the ring cleavage, temporary light exposure of cetylpiridinium chloride solutions, typically before rheological tests, can have additive effects. After several weeks, samples will acquire a slight yellow coloring evidencing the photochemical reactions. Such samples would contain impurities, mostly aldehyde enamine and hexadecane fatty chains. Some or all of those impurities can demix with the rest of the solution and can produce slip layers responsible for the abnormal shear-banding dynamics described for the O-OS and IS.

Acknowledgments

The authors thanks S. Asnacios, J.F. Berret, O. Cardoso, V. Grenard and P. Lettinga for fruitful discussions, and the ANR JCJC-0020 for financial support. M.A.F thanks N. Turro for his advices on the photochemistry. M.A.F. thanks the Fulbright Commission for its support.

[1] P.D. Olmsted, *Rheol. Acta* **47**, 283-300 (2008).
[2] J.F. Berret, Rheology of wormlike micelles : Equilibrium properties and shear-banding transition, Molecular gels, Elsevier (2005).
[3] S. Lerouge and J.F. Berret, Shear-Induced Transitions and Instabilities in Surfactant Wormlike Micelles, *Advances in Polym. Sci.* **230**, 1-71, Springer (2010).
[4] S. Manneville *et al.*, *Phys. Rev. E* **75**, 061502 (2007).
[5] J. Sprakel *et al.*, *Soft Matter* **4**, 1696-1705 (2008).
[6] P. Coussot *et al.*, *Phys. Rev. Lett.* **88**, 218301 (2002).
[7] L. Bécu *et al.*, *Phys. Rev. Lett.* **96**, 138302 (2006).
[8] F. Ianni *et al.*, *Phys. Rev. E* **77**, 031406 (2008).
[9] T. Gibaud, C. Barentin and S. Manneville, *Phys. Rev. Lett.* **101**, 258302 (2008).
[10] P. C. F. Møller *et al.*, *Phys. Rev. E* **77**, 041507 (2008).
[11] S. A. Rogers *et al.*, *Phys. Rev. Lett.* **100**, 128304 (2008).
[12] GDR Midi, *Eur. Phys. J. E* **14**, 341-365 (2004).
[13] C. Gilbreth *et al.*, *Phys. Rev. E* **74**, 051406 (2006).
[14] J.-B. Salmon *et al.*, *Phys. Rev. Lett.* **90**, 228303 (2003).
[15] S.M. Fielding, *Soft Matter* **2**, 1262-1279 (2007).
[16] S. Manneville, *Rheol. Acta* **47**, 301-318 (2008).
[17] P.T. Callaghan, *Rheol. Acta* **47**, 243-255 (2008).
[18] M.R. Lopez-Gonzalez *et al.*, *Phys. Rev. Lett.* **93**, 268302 (2004).
[19] M.P. Lettinga and S. Manneville, *Phys. Rev. Lett.* **103**, 248302 (2009).
[20] K.W. Feindel and P.T. Callaghan, *Rheol. Acta* **49**, 1003-1013 (2010).
[21] J.M. Adams, S.M. Fielding and P.D. Olmsted, *J. Non-Newt. Fluid Mech.* **151**, 101-118 (2008).
[22] S. Lerouge *et al.*, *Phys. Rev. Lett.* **96**, 088301 (2006).
[23] S. Lerouge *et al.*, *Soft Matter* **4**, 1808-1819 (2008).
[24] M.A. Fardin *et al.*, *Phys. Rev. Lett.* **103**, 028302 (2009).
[25] M.A. Fardin *et al.*, *Phys. Rev. Lett.* **104**, 178303 (2010).
[26] A. Groisman and V. Steinberg, *Nature* **405**, 53 (2000).
[27] A. Groisman and V. Steinberg, *New J. Phys.* **6**, 29 (2004).
[28] S. Majumdar and A.K. Sood, *et al.*, *Phys. Rev. E* **84**, 015302 (2011).
[29] A.N. Morozov and W.van Saarloos, *Physics Reports* **447**, 112-143 (2007).
[30] S.M. Fielding, *Phys. Rev. E* **76**, 016311 (2007).
[31] S.M. Fielding, *Phys. Rev. Lett.* **104**, 198303 (2010).
[32] A. Nicolas and A. N. Morozov, submitted to *Phys. Rev. Lett.* (2011).
[33] O. Radulescu and P.D. Olmsted, *Rheol. Acta* **38**, 606-613 (1999).
[34] C-Y.D. Lu, P.D. Olmsted and R.C. Ball, *Phys. Rev. Lett.* **84**, 642-645 (2000).
[35] O. Radulescu and P.D. Olmsted, *J. Non-Newt. Fluid Mech.* **91**, 141-162 (2000).
[36] O. Radulescu *et al*, *Europhys. Lett.* **62**, 230-236 (2003).
[37] J. F. Berret, D. C. Roux, and G. Porte., *J. Phys. II France* **4**, 1261-1279 (1994).
[38] J.F. Berret, G. Porte and J.P. Decruppe, *Phys. Rev. E* **55**, 1668-1676 (1997).
[39] W.M. Holmes, M.R. Lopez-Gonzales, and P.T. Callaghan, *Eur. Phys. Lett.* **64**, 274-280 (2003).
[40] M.R. Lopez-Gonzales, W.M. Holmes and P.T. Callaghan, *Soft Matter* **2**, 855 (2006).
[41] M.M. Britton and P.T. Callaghan, *Eur. Phys. J. B* **7**, 237-249 (1999).
[42] K.E. Wilzbach and D.J. Rausch, *J. Am. Chem. Soc.* **92**, 2178-2179 (1970).
[43] J.C. Andre *et al.*, *J. Chem. Educ.* **54**, 387-388 (1977).
[44] E. Vaganova *et al.*, *J. Fluorescence* **12**, 219-224 (2002).
[45] S. Manneville, L. Bécu, and A. Colin, *Eur. Phys. J. AP* **28**, 361-373 (2004).
[46] S. Lerouge, J. P. Decruppe, and J. F. Berret, *Langmuir* **16**, 6464-6474 (2000).
[47] J. F. Berret, *Langmuir* **13**, 2227-2234 (1997).
[48] C. Grand, J. Arrault, and M. E. Cates, *J. Phys. II France* **7**, 1071-1086 (1997).
[49] S. Lerouge, J. P. Decruppe, and P. D. Olmsted, *Langmuir* **20**, 11365 (2004).
[50] J. P. Decruppe, S. Lerouge and J. F. Berret, *Phys. Rev. E* **63**, 022501 (2001).
[51] Q.B. Shubert, N.J. Wagner, E.W. Kaler, S.R. Raghavan,

Langmuir **20**, 3564-3573 (2004).
[52] Y.T. Hu and A. Lips, *J. Rheol.* **49**, 1001-1027 (2005).
[53] M.A. Fardin *et al.*, *Eur. Phys. Lett.* **96**, 44004 (2011).
[54] C.D. Andereck *et al.*, *J. Fluid Mech.* **164**, 155 (1986).
[55] R.G. Larson *et al.*, *J. Fluid Mech.* **218**, 573-600 (1990).
[56] B.M. Baumert and S.J. Muller, *Rheol. Acta* **34**, 147 (1995).
[57] N. Abcha *et al.*, *Exp. Fluids* **45**, 85 (2008).
[58] L. Bécu, D. Anache, S. Manneville, A. Colin, *Phys. Rev. E* **76**, 011503 (2007).
[59] E. Fischer and P.T. Callaghan, *Phys. Rev. E* **64**, 011501 (2001).
[60] M.A. Fardin *et al.*, in preparation.
[61] M.E. Cates and S.J. Candau, *J. Phys.: Condens. Matter* **2**, 6869-6892 (1990).
[62] J.P. Decruppe *et al.*, *Phys. Rev. E* **73**, 061509 (2006).
[63] M.E. Hegelson *et al.*, *J. Rheol.* **53**, 727 (2009).
[64] A. Raudsepp and P.T. Callaghan PT, *Soft Matter* **4**, 784-796 (2008).
[65] E. Fischer and P. T. Callaghan, *Europhys. Lett.* **50**, 803-809 (2000).
[66] O.I. Vinogradova and A.V. Belyaev, *J. Phys.: Condens. Matter* **23**, 184104 (2011).
[67] P.G. de Gennes, *C.R. Acad. Sc. Paris* **288**, 219-220 (1979).
[68] M.A. Fardin *et al.*, *Soft Matter* DOI: 10.1039/C1SM06165H (2012).
[69] P. Pakdel *et al.*, *Phys. Rev. Lett.* **77**, 2459-2462 (1996).
[70] B. Lasne, Thèse de Doctorat, Université Paris-Diderot, unpublished (2010).
[71] R. Ganapathy and A. K. Sood, *Phys. Rev. Lett.* **96**, 108301 (2006).
[72] R. Ganapathy, S. Majumdar, and A. K. Sood, *Phys. Rev. E* **78**, 021504 (2008).
[73] R. Ganapathy, S. Majumdar, and A. K. Sood, *Eur. Phys. J. B* **64**, 537-542 (2008).
[74] L. Bécu, S. Manneville and A. Colin, *Phys. Rev. Lett.* **93**, 018301 (2004).
[75] C. Dimitriou *et al.*, *Rheol. Acta* accepted.